Downloaded from http://sp.lyellcollection.org/ at Pennsylvania State University on September 16, 2016

Stability of chloritoid + biotite-bearing assemblages in some metapelites from the Palaeoproterozoic Singhbhum Shear Zone, eastern India and their implications

NANDINI SENGUPTA

Department of Geology, University of Calcutta, 35 Ballygunge Circular Road, Kolkata 700019, India (e-mail: nandinisg@yahoo.com)

Abstract: The arcuate Singhbhum Shear Zone (SSZ) of the East Indian Shield area, fringing the Archaean Singhbhum Craton, exposes a mélange-like ensemble of polymetamorphosed and highly tectonized siliciclastic sediments, mafic–ultramafic extrusive, tourmaline-rich rocks, magnetite–apatite rocks, granites and Cu–Fe–U sulphide ores of Meso- to Palaeoproterozoic age (1.5–1.77 Ga). Metapelites from two localities in the SSZ developed the enigmatic assemblage chloritoid–biotite–garnet–chlorite, which are the first reported from India and the eighth in world occurrence. Textural studies and algebraic analyses of the phase compositions in the KFMASH system indicate the operation of the reaction, chloritoid + biotite → garnet + chlorite + H_2O and this reaction has a negative slope in pressure–temperature (P–T) space. Quantitative geothermobarometry and pseudosections in the NCMnKFMASHO system indicate that this reaction occurred during prograde metamorphism that culminated at 6.3 ± 1 kbar and 490 ± 40 °C. The stability of the chloritoid + biotite is also sensitive to the MnO content of the bulk rock, and to the chemical potential of H_2O and oxygen (μ_{H_2O} and μ_{O_2}, respectively), of the ambient fluid phase. Thrusting of continental crust in a collisional setting is invoked to explain the peak metamorphic temperatures and the clockwise P–T trajectory is construed from the petrological study of the chloritoid–biotite schist.

Petrological characterization of metapelitic rocks occurring in the fold belts peripheral to one or more cratonic blocks is used as a common marker to decipher the complex geological history and tectonic setting in many terrains, particularly those experiencing medium-grade metamorphism (Harte & Hudson 1979; Labotka 1980, 1981; Wang & Spear 1991; Ganguly *et al.* 2000; Goscombe *et al.* 2003; Mahato *et al.* 2008; Dasgupta *et al.* 2009; Sharma 2010). Although a large number of studies on the petrology of medium-grade pelites across the world have been published, there exist only seven localities where pelites record the four AFM phases garnet–chlorite–chloritoid–biotite (Droop & Harte 1995). Evolution of pelites with these four phases is a subject of considerable debate owing to contrasting topologies proposed for the assemblage garnet–muscovite–chlorite–biotite–chloritoid–quartz–vapour in the KFMASH (K_2O–FeO–MgO–Al_2O_3–SiO_2–H_2O) system (Droop & Harte 1995). The KFMASH topology of Harte & Hudson (1979), which is supported by Droop & Harte (1995), assumes a steep positive pressure–temperature (P–T) slope of the KFMASH univariant reaction (Als, St): garnet + chlorite + muscovite = chloritoid + biotite + quartz + H_2O with garnet + chlorite placed on the lower-temperature side of the reaction. The thermodynamically computed KFMASH topology of Spear & Cheney (1989), although supporting the positive slope of the reaction (Als, St), places the garnet + chlorite + H_2O on the higher-temperature side of the reaction.

The Singhbhum Shear Zone that separates the Archaean Singhbhum Craton from the Palaeo- to Meso-Proterozoic North Singhbhum Fold Belt (Fig. 1) exposes chloritoid–biotite schist containing the enigmatic mineral assemblage garnet–chlorite–chloritoid–biotite. The stability and rarity of this particular assemblage in nature cannot be explained with the help of the topological arrangement described in existing KFMASH petrogenetic grids. Other than studying the characteristics of stability of chloritoid + biotite v. garnet + chlorite, this paper attempts to:

(a) to decipher the paragenetic relationship between chloritoid and the associated minerals present in the metapelitic rocks of the studied area;
(b) to place constraints on the pressure–temperature conditions under which such enigmatic mineral assemblage formed;
(c) to construct an alternative schematic KFMASH petrogenetic grid to explain the stability and mutual relationship between chloritoid and the associated minerals in P–T space;
(d) to evaluate the control to the bulk chemical composition of metapelites, and the chemical

From: MAZUMDER, R. & SAHA, D. (eds) 2012. *Palaeoproterozoic of India*. Geological Society, London, Special Publications, **365**, 91–116. http://dx.doi.org/10.1144/SP365.6 © The Geological Society of London 2012. Publishing disclaimer: www.geolsoc.org.uk/pub_ethics

Downloaded from http://sp.lyellcollection.org/ at Pennsylvania State University on September 16, 2016

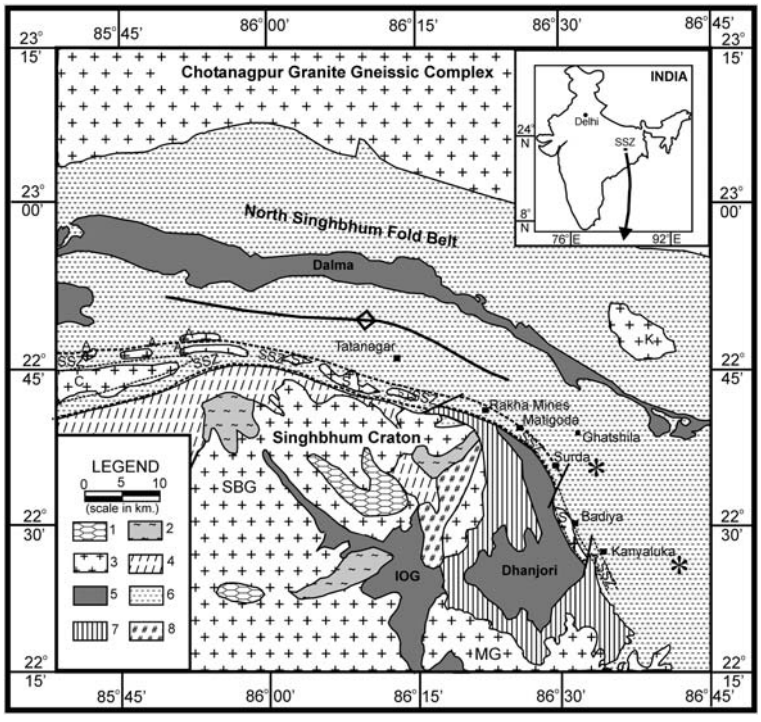

Fig. 1. Geological map showing the distribution of stratigraphic units in parts of eastern India after Saha (1994): 1, Older Metamorphic Group Granite; 2, Older Metamorphic Tonalitic Gneiss; 3, Granite (A, Arkasani Granite Gneiss and Granophyre; C, Chakradharpur Granite Gneiss; K, Kuilapal Granite; MG, Mayurbhanj Granite; S, Soda Granite; SBG, Singhbhum Granite); 4, Iron Ore Group shale, tuff and phyllite; 5, Basic lava and intrusives (Dalma, Dalma Group of volcanics; Dhanjori, Dhanjori Group of metabasic rocks; IOG, Iron Ore Group volcanics); 6, pelites and psammopelites of the Singhbhum Group; 7, Dhanjori Group metasediments; 8, Proterozoic gabbro-anorthosite; SSZ, Singhbhum Shear Zone; the locations marked with a star exposes the four-phase assemblage chloritoid–biotite–garnet–chlorite.

potentials of H_2O and O_2 (μ_{H_2O} and μ_{O_2}, respectively) on the stability of the mineral assemblage;

(e) to understand the effect of the construed P–T path in the light of an existing tectonic model.

Geological setting

The North Singhbhum Fold Belt (NSFB), the arc-shaped belt of Palaeo- to Meso-Proterozoic age, is sandwiched between the 3–3.4 Ga old Singhbhum Craton containing granitoids and minor supracrustal rocks in the south and the Meso- to Neo-Proterozoic Chotanagpur Granite Gneiss Complex in the north (Fig. 1) (Sharma *et al.* 1994; Sarkar 2000; Sengupta *et al.* 2005; Mahato *et al.* 2008; Chatterjee *et al.* 2010). The NSFB, which is dominated by metasediments, contains two mafic–ultramafic suites interstratified with metasedimentary rocks: the Dhanjori Formation to the south and the Dalma volcanics at the axial part of the belt (Fig. 1). The more than 150 km-long arc-shaped Singhbhum Shear Zone (SSZ) of variable width (*c*. 0.5–5.0 km) separates the NSFB from the Singhbhum Craton. The SSZ, which is developed along the northern boundary of the Singhbhum Craton and northeastern fringe of the Dhanjori Formation exposes an ensemble of laterally discontinuous lithologies including kyanite–quartzite and kyanite–mica schist, metapelitic and psammopelitic rocks, amphibole + chlorite ± talc schist, apatite–magnetite rock, conglomerate, tourmalinite and mylonitized granite resembling a tectonic mélange (Sarkar 2000; Sengupta *et al.* 2005). These rocks are highly tectonized with extensive development of mylonites and phyllonites with typical S–C fabric and various shear markers (Sarkar 1984; Ghosh & Sengupta 1987, 1990; Mukhopadhyay & Deb 1995; Sengupta *et al.* 2005). Kinematic shear indicators in the SSZ indicate the thrusting of the rocks of the NSFB over the Singhbhum Craton (Fig. 1). Important

Downloaded from http://sp.lyellcollection.org/ at Pennsylvania State University on September 16, 2016

economic deposits of Fe, Cu, U and other non-metallic minerals, such as kyanite and apatite, are present along this zone (Sarkar 2000).

Limited geochronological data suggest that sediments of the NSFB were deposited after 2.2 Ga (Mahato *et al.* 2008), which was followed by mafic magmatism of the Dhanjori Formation at around 2.1 Ga (Roy *et al.* 2002; Mahato *et al.* 2008). Subsequently, in the SSZ, the supracrustal rocks underwent multiple episodes of folding and shearing over a protracted period from about 1.7 to 1.3 Ga in response to regional compression that acted perpendicular to the trend of the SSZ (Ghosh & Sengupta 1990; Mukhopadhyay & Deb 1995; Sarkar 2000; Sengupta *et al.* 2005; Mahato *et al.* 2008). Vestiges of approximately 0.8 Ga age have recently been documented from a few places in the eastern part of the NSFB (Chatterjee *et al.* 2010). Detailed structural and limited petrological studies of the rocks of the SSZ have identified three major phases of deformation (D_1, D_2 and D_3) and two phases of metamorphism (M_1 and M_2), with a major phase of shearing broadly coeval with the D_2 event (Bandyopadhyay 2003; Sengupta *et al.* 2005). The approximately 1.5–1.8 Ga U–Pb date of uraninite is believed to be the time of occurrence of the major shearing event and, hence, the time that the D_2 deformation occurred in the SSZ (Rao & Rao 1983). The M_1 metamorphism in the SSZ is marked by the formation of porphyroblasts (e.g. garnet, chloritoid, staurolite and kyanite) in metapelites and psammopelites that developed syn- to post-tectonically with the regional schistosity and/or shear foliation (S_2) related to the D_2 deformation. M_2 is marked by retrogressive metamorphism and is correlated with the D_3 deformational event. Upper-greenschist- to amphibolite-facies metamorphic conditions have been inferred from the assemblages of the porphyroblastic minerals in pelitic and psammopelitic rocks of the SSZ (Sarkar 2000; Bandyopadhyay 2003; Sengupta *et al.* 2005).

Chloritoid–biotite schist has been found to occur in two localities of the SSZ (Surda and Kanyaluka: Fig. 1) and is the subject of the present communication. The colour of chloritoid–biotite schist varies from pale to dark grey depending on the proportions of garnet, chloritoid, magnetite, muscovite, chlorite and biotite. The rock exposed near Kanyaluka is dark grey in colour owing to the large proportion of magnetite (Fig. 2a). The rocks occurring in the close vicinity to the chloritoid–biotite schist include kyanite–quartzite, kyanite–mica schist, sheared granite and thinly banded psammopelitic schist. A set of schistosity defined by the alternate banding of muscovite and biotite is the dominant planar fabric of the studied area (Fig. 2a). The schistosity, which is phyllonitic in places, marks the S_2 foliation plane. Because of intense shearing, sets of earlier schistosity (S_1) and primary bedding planes (S_0) are rarely observed on the meso-scale. Commonly, the S_2 fabric bent around nodular aggregates of porphyroblastic chloritoid, quartz and magnetite (Fig. 2b). In places, randomly oriented needles of chloritoid occur in the schistose micaceous matrix (Fig. 2c). Porphyroblastic garnet has an euhedral outline and appears to grow under static condition (Fig. 2d).

Mineral assemblages and petrography

Several samples of chloritoid–biotite schist have been collected from two areas, namely Surda and Kanyaluka, in the SSZ (Fig. 1). For quantitative geothermobarometry and to place constraints on the stability of the rare chloritoid + biotite-bearing assemblages, samples from the psammopelites exposed in adjoining areas that share a common metamorphic evolution with the chloritoid–biotite schist are also chosen for the present study. After routine microscopic study of all the collected samples, representative thin sections have been studied:

- to recognize any variation in the chloritoid-bearing assemblages present in the studied area;
- to understand mutual textural relationships between chloritoid and other KFMASH minerals;
- to select samples for detailed chemical analyses from the chloritoid–biotite schist and psammopelitic schist.

Minerals present in the chloritoid–biotite schist and in the psammopelitic schist are listed in Table 1. On the basis of mineralogy, three associations, namely A (Cld + Bt + Grt + Chl), B (Cld + Bt + Grt), C (Cld + Bt + Chl), are recognized in the chloritoid–biotite schist. In all the three associations, flakes of biotite and muscovite define a prominent schistosity (S_2) (Fig. 3a). Laths of chlorite athwart the schistosity are common. The same schistosity is also traceable and is the prominent planar fabric in the adjoining psammopelitic schist. Garnet (Association A and B) and chloritoid (Association A, B and C) form porphyroblasts in chloritoid–biotite schist. Commonly, chloritoid blades are flattened parallel to the schistosity and bear the impression of deformation manifested by undulose extinction, and the development of kinks (Fig. 3b–e) and fractures perpendicular to the length of grain (Fig. 3c). The schistosity swerves around the chloritoid porphyroblasts in places (Fig. 3d). Rarely, inclusions of quartz in chloritoid define an internal fabric (S_i-trail) that is parallel with the external schistosity (S_e) defined by mica (Fig. 3c). In places, twinned

Downloaded from http://sp.lyellcollection.org/ at Pennsylvania State University on September 16, 2016

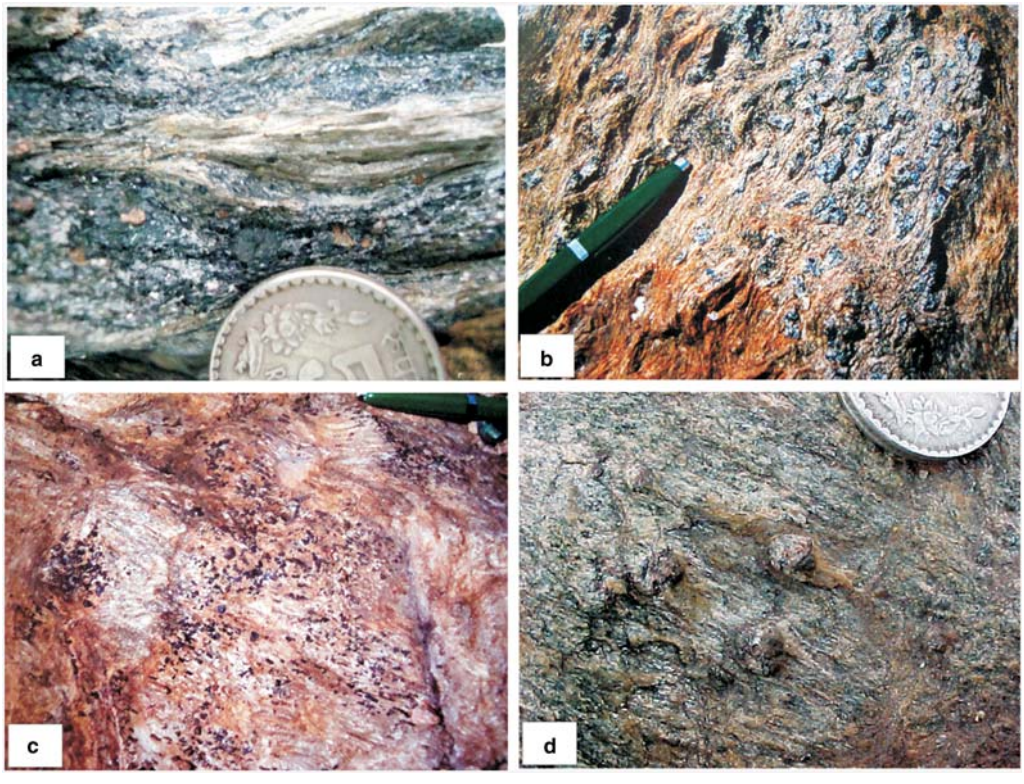

Fig. 2. (**a**) Outcrop photograph of schistosity (S_2) in chloritoid–biotite schist defined by alternate muscovite-rich and biotite-rich banding. (**b**) Outcrop photograph of schistosity swerves around nodular chloritoid porphyroblasts. (**c**) Outcrop photograph of randomly oriented needles of chloritoid in schistose micaceous matrix. (**d**) Outcrop photograph of euhedral garnet porphyroblasts in chloritoid–biotite schist.

chloritoid grains that impinge into the foliation include polygonal aggregates of quartz (Fig. 3e). Garnet porphyroblasts commonly show an euhedral outline and appear to grow over the schistosity defined by mica and the elongated chloritoid (Fig. 3c, d, f). The pervasive schistosity abruptly stops at the euhedral faces of garnet (Fig. 3c, d, f). Locally, garnet porphyroblasts contain inclusions of chloritoid laths (Fig. 4a). Volumetrically minor chlorite flakes athwart the schistosity, cross-cut

Table 1. *Mineral associations in the chloritoid–biotite schist and the psammopelitic schist*

Rock type	Association	Sample no.	Area	AFM phases	Accessory minerals
Chloritoid–biotite schist	A	L5A (1–6)	Surda	Grt + Chl + Cld + Bt	Tur + Ilm + Zrn
		K3CG (1–8)	Kanyaluka	Grt + Chl + Cld + Bt	Mag + Ilm + Tur + Ap + Zrn
		24C (1–1a)	Kanyaluka	Grt + Chl + Cld + Bt	Mag + Ilm + Tur + Ap + Zrn
	B	L5X (1–3)	Surda	Grt + Cld + Bt	Mag + Ilm + Ap + Zrn
		K3 (1–6)	Kanyaluka	Grt + Cld + Bt	Mag + Ilm + Ap + Zrn
	C	K5 (1–2)	Kanyaluka	Cld + Bt + Chl	Ap + Mag + Zrn
Psammo-pelitic schist	D	H2q (1–8)	Matigoda	Grt + Bt + Chl + Plag	Ep + Tur + Mag + Ilm
		H2m (1–4)	Matigoda	Grt + Bt + Chl + Plag	Ep + Tur + Mag + Ilm
		G2 (1–5)	Rakha Mines	Grt + Bt + Chl + Plag	Ep + Zo + Tur + Mag + Ilm
	E	16A (1–5)	Badiya	Grt + Bt + Plag	Ap + Ep + Tur + Mag + Ilm + Sulphides

Note: All of the associations include quartz and muscovite; the mineral abbreviations used in this communication are after Kretz (1983).

Downloaded from http://sp.lyellcollection.org/ at Pennsylvania State University on September 16, 2016

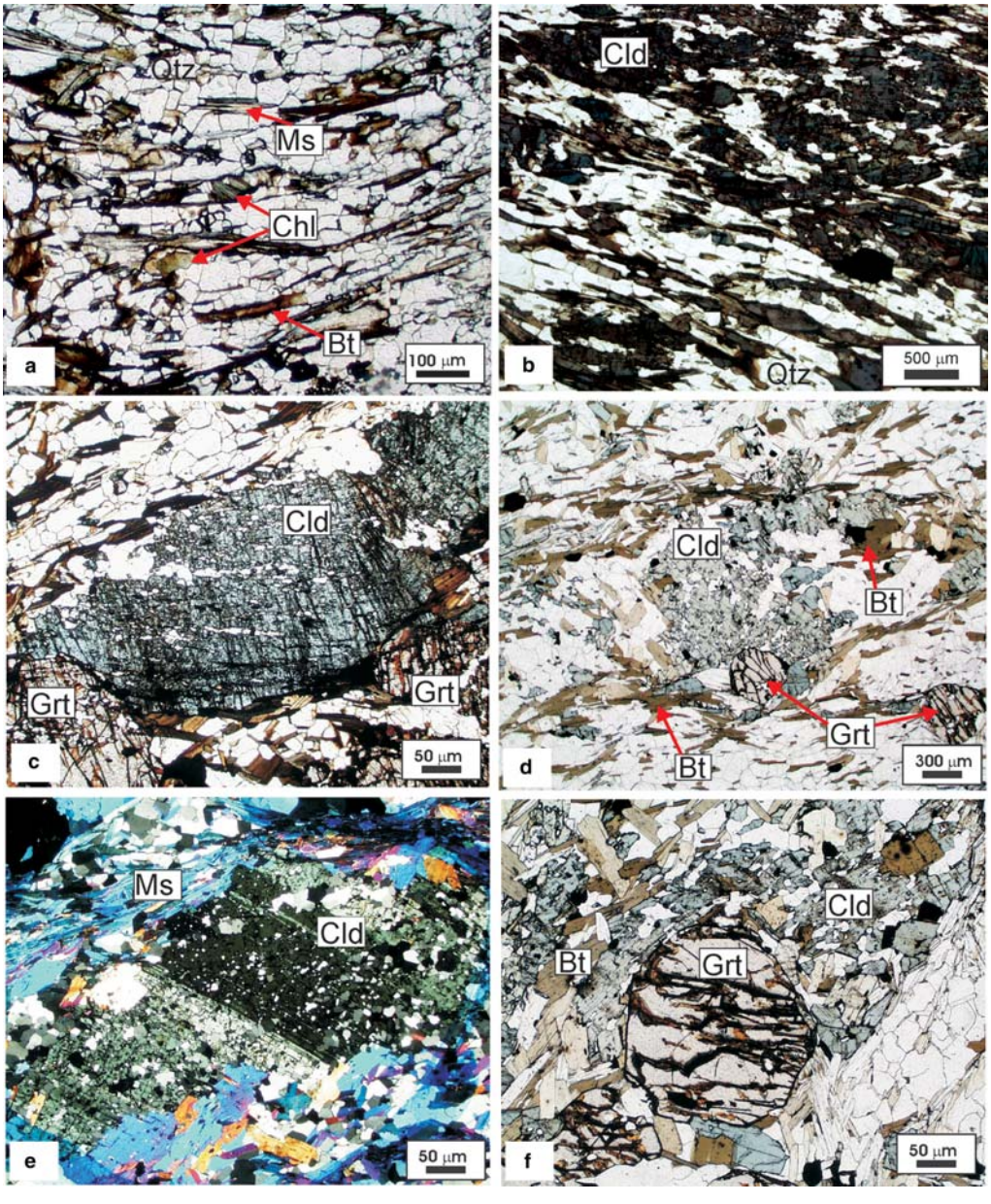

Fig. 3. (**a**) Photomicrograph of needles of muscovite and biotite, together with the elongated polygonal grains of quartz, define the schistosity (S_2) and laths of chlorite in places athwart the schistosity. (**b**) Photomicrograph of deformed and fractured grains of chloritoid in parallelism with the S_2. (**c**) Photomicrograph of quartz inclusions defining the S_i-trail within chloritoid is parallel to S_2. (**d**) Photomicrograph of S_2 swerves around rounded porphyroblasts of chloritoid. (**e**) Photomicrograph (in cross-polarized light) of chloritoid grains showing lamellar twining and also bearing a S_i-trail parallel to S_2. (**f**) Photomicrograph of an euhedral grain of garnet overprinted upon schistosity defined by chloritoid. Photomicrographs (a), (b), (c), (d) and (f) are taken in plane-polarized light. All of the mineral abbreviations used in this paper are after Kretz (1983).

both by biotite laths (Fig. 4b–d) and chloritoid blades (Fig. 4c). In places, small prisms of chloritoid are engulfed within chlorite flakes (Fig. 4d). Magnetite occurs in two modes. Commonly, euhedral and subhedral magnetite grains are scattered in the matrix, and show intergrowth with chloritoid

Downloaded from http://sp.lyellcollection.org/ at Pennsylvania State University on September 16, 2016

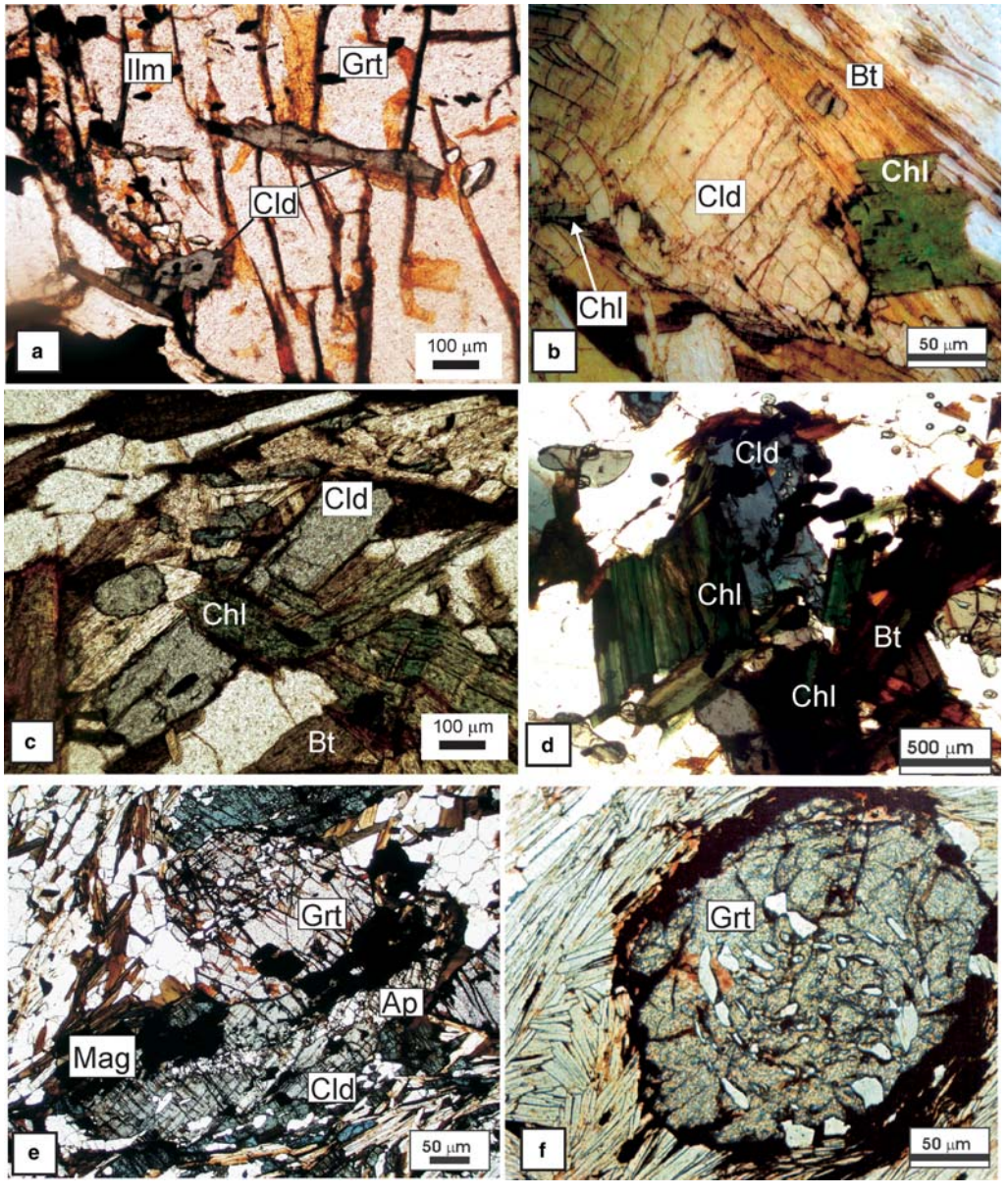

Fig. 4. (**a**) Photomicrograph showing inclusions of chloritoid and ilmenite within garnet. (**b**) Laths of chlorite cross-cuts biotite needles. (**c**) Photomicrograph of laths of chlorite cross-cutting a chloritoid blade. (**d**) Photomicrograph of a grain of chloritoid engulfed within flakes of chlorite. (**e**) Photomicrograph showing two sets of shear foliation ($S-C$ fabric) around the garnet porphyroblast: one set is defined by needles of biotite running in the NW corner of the photomicrograph; and another set is defined by white mica, biotite and chloritoid blades aligned in the lower half of the photomicrograph. Veins of apatite parallel to the shear foliation passes through the large blade of chloritoid, and magnetite is aligned along the boundary between garnet and chloritoid. (**f**) Photomicrograph of a relict fold defined by earlier schistosity (S_1) in a matrix with a similar pattern to that of the sigmoid S_i-trail within the core of garnet; the rim of garnet is devoid of inclusions. All of the above photomicrographs are taken in plane-polarized light.

(Fig. 4e). Magnetite, in the other mode, occurs as inclusions in garnet and chloritoid porphyroblasts. Apatite occurs in the matrix either as isolated grains or as cluster of smaller grains. Locally, veins of apatite cross-cut chloritoid porphyroblasts (Fig. 4e). The textural features indicate that

Downloaded from http://sp.lyellcollection.org/ at Pennsylvania State University on September 16, 2016

chloritoid grew broadly syntectonic to the schistosity, whereas garnet and chlorite formed under static conditions after the schistosity-forming stress withdrew or significantly waned out. From this, it follows that chloritoid and biotite are paragenetically older than both garnet and chlorite.

In the psammopelitic schist, muscovite, biotite, chlorite (when present) define the schistosity (S_2). In places, folded traces of an earlier schistosity (S_1) defined by muscovite is observed (Fig. 4f). Quartz and plagioclase form polygonal aggregates in the matrix. Garnet occurs as porphyroblasts. The core of garnet is studded with quartz inclusions that define a sigmoidal pattern (Fig. 4f). The rims of the garnet porphyroblasts show a euhedral outline and are practically devoid of inclusion (Fig. 4f). Like the chloritoid–biotite schist, the external schistosity sharply abuts against the euhedral face of garnet. This feature suggests that garnet grew in two stages. The growth of garnet started at the time of formation of the schistosity (the core), whereas the final growth of garnet (the rim) outlasted deformation and, hence, post-dated the schistosity.

Mineral chemistry

The compositions of minerals in the studied rocks were determined with a CAMECA SX51 electron probe microanalyser at the Mineralogisch Petrologisches Institut, Bonn University. Wavelength Dispersive Spectrometry (WDS) analyses were performed using an accelerating voltage of 15 kV, a current of 5.10 A and a 1–2 μm-diameter electron beam. For muscovite and plagioclase, the electron beam was broadened to 5–10 μm (diameter) to avoid alkali loss. The following well-calibrated standards were used: F = BaF_2; Na, Ca and Si = jadeite–diopside glass; Mg = MgO; Al = Al_2O_3; Fe = pure Fe; K = sanidine; Ti = TiO_2; Cr = pure Cr; and Mn = Mn with a Fe-mixture. The raw data were processed using the PAP procedure (Pouchou & Pichoir 1984). At least three points from each individual grain and at least five grains were analysed from each thin section for minerals that are not chemically zoned. At least five pairs of core and rim from each grain were analysed to detect the presence of chemical zoning. In some sections, garnet porphyroblasts were traversed at the interval of 50–100 μm to check the compositional variation or zoning from core to rim. Representative compositions of the minerals are presented in Tables 2–7.

None of the minerals in the chloritoid–biotite schist shows significant compositional zoning. Chloritoid in all the chloritoid–biotite schist is extremely Fe-rich (Mg concentration $X_{Mg} = Mg/(Mg + Fe^{2+}) = 0.077–0.141$) with chloritoid in Association C being most magnesian (X_{Mg} goes up to 0.141: Table 2). The levels of Fe^{3+} in the chloritoid analyses that were recalculated following the procedure of Chopin *et al.* (1992) are low (0.00–0.07 apfu (atoms per formula unit)).

Biotite in the chloritoid–biotite schist is more magnesian (X_{Mg}: 0.363–0.410, Table 3) compared to the coexisting chloritoid. The TiO_2 content of biotite was found to vary between 0.50 and 1.72 wt% (Table 3), while biotite in the ilmenite-bearing samples has a higher TiO_2 content (>1 wt%) than the ilmenite-free samples (<0.6 wt%). Biotite in psammopelitic schist is more magnesian (X_{Mg}: 0.42–0.51) and titanian (TiO_2: 1.71–2.95 wt%, Table 3) than that of chloritoid–biotite schist.

Garnet in chloritoid–biotite schist is rich in almandine (77.0–94.9 mol%, Table 4). Garnet in all the associations from chloritoid–biotite schist (A & B) shows a very low concentration of grossular and spessartine molecules (sum of the two never exceeds the range 1.21–5.21 mol%); barring one sample of Association A (#L5A/2), which contains garnet with a higher content of spessartine (3.89–4.94 mol%) and grossular (11.81–12.70 mol%). Garnet is slightly less magnesian ($X_{Mg} = Mg/(Mg + Fe^{2+})$: 0.036–0.065) than the coexisting chloritoid. In contrast to chloritoid–biotite schist, the garnet core in the psammopelitic schist has a distinctly higher spessartine (11.01–27.63 mol%) and grossular (9.56–15.81 mol%) content. Strongest compositional zoning in garnet is noted in one set of samples (#H2q/1), where the spessartine content drops significantly from the core to the rim of garnet (core 12.67 mol%; rim 1.79 mol%). No significant variation in terms of grossular content was, however, noted from the core to the rim of garnet (Table 4).

In chloritoid–biotite schist, X_{Mg} of chlorite shows insignificant variation (0.367–0.400). Following the trends of biotite and chloritoid, chlorite in association C is marginally more magnesian (X_{Mg}: 0.373–400) than chlorite in Association A (X_{Mg}: 0.367–0.375). Chlorite in psammopelitic schist is distinctly more magnesian (X_{Mg}: 0.424–0.488) than the chlorite in chloritoid–biotite schist (Table 5). In psammopelitic schist, both primary chlorite and secondary retrograde chlorite are present, but there is no compositional variation among them.

Muscovite shows a considerable amount of phlogopite–annite, celadonite, pyrophyllite, margarite and paragonite. Together, they vary within the ranges of 21.16–30.51 and 29.95–34.44 mol% in chloritoid–biotite schist and psammopelitic schist, respectively. Muscovite in psammopelite has distinctly higher paragonite (11.86 ± 4.47 mol%)

Downloaded from http://sp.lyellcollection.org/ at Pennsylvania State University on September 16, 2016

Table 2. *Representative analyses of chloritoid from Associations A–C*

Association	A				B				C	
Sample no.	L5A/1		K3CG/1		L5X/1		K3/1		K5/1	
	core	rim	core	rim	core	rim	core	rim	core	rim
SiO_2	24.91	24.72	23.94	23.77	23.97	23.67	24.04	23.83	25.21	24.57
TiO_2	0.01	0.01	0.10	0.25	0.02	0.00	0.25	0.36	0.01	0.03
Al_2O_3	39.94	40.06	41.69	40.87	40.37	40.45	41.02	41.25	41.44	40.78
Cr_2O_3	0.00	0.00	0.02	0.05	0.06	0.00	0.03	0.01	0.05	0.03
FeO	24.97	25.17	25.44	25.95	26.04	25.98	25.91	25.64	22.96	24.06
MnO	0.23	0.16	0.04	0.03	0.02	0.03	0.05	0.08	0.08	0.14
MgO	2.08	2.06	1.44	1.49	1.77	1.75	1.22	1.35	2.11	2.02
CaO	0.00	0.00	0.01	0.01	0.01	0.03	0.01	0.02	0.03	0.07
Na_2O	0.03	0.03	0.14	0.11	0.00	0.00	0.12	0.11	0.12	0.13
K_2O	0.01	0.00	0.02	0.02	0.00	0.03	0.01	0.02	0.01	0.01
Total	92.19	92.22	92.84	92.55	92.26	91.94	92.66	92.67	92.02	91.84
Si	2.063	2.049	1.976	1.976	1.996	1.980	1.994	1.974	2.062	2.033
Ti	0.001	0.001	0.006	0.016	0.001	0.000	0.016	0.022	0.000	0.002
Al	3.900	3.914	4.057	4.006	3.964	3.990	4.011	4.030	3.996	3.979
Cr	0.000	0.000	0.001	0.003	0.004	0.000	0.002	0.001	0.004	0.002
Fe^{2+}	1.694	1.709	1.756	1.804	1.780	1.789	1.797	1.777	1.570	1.665
Fe^{3+}*	0.035	0.035	0.000	0.000	0.034	0.028	0.000	0.000	0.000	0.000
Mn	0.016	0.011	0.003	0.002	0.001	0.002	0.003	0.005	0.005	0.010
Mg	0.257	0.255	0.177	0.185	0.220	0.218	0.150	0.166	0.257	0.249
Ca	0.000	0.000	0.001	0.001	0.001	0.003	0.001	0.002	0.003	0.006
Na	0.005	0.005	0.023	0.018	0.000	0.000	0.020	0.018	0.019	0.021
K	0.001	0.000	0.002	0.003	0.000	0.003	0.001	0.003	0.001	0.001
Σcation	7.972	7.979	8.002	8.014	8.001	8.013	7.994	7.998	7.918	7.968
X_{Mg}	0.132	0.130	0.091	0.093	0.110	0.109	0.077	0.086	0.141	0.130

Note: *Fe^{3+} recalculation after Chopin *et al.* (1992), $X_{Mg} = Mg/(Mg + Fe^{2+})$; cation recalculation on 12(O).

than muscovite in chloritoid–biotite schist (7.53 ± 1.66 mol%) (Table 6).

Plagioclase composition that is restricted to psammopelite varies with in An_{19}–An_{29}, although no compositional zoning was noted in a single grain (Table 7).

Thermobarometric calculation

For quantitative temperature estimates of the studied rocks, a number of geo-thermometers (Table 4) were applied to the mineral assemblages in chloritoid–biotite schist and psammopelitic schist in the adjoining localities. Pressure was computed using the assemblage garnet–biotite–plagioclase–quartz (GBPQ: Wu *et al.* 2004) and garnet–muscovite–plagioclase–quartz (GMPQ: Wu & Zhao 2006) in psammopelitic schist. To minimize the problem of kinetic inhibition, estimates were carried out using ferromagnesian minerals that were either touching each other or occurred within 10–15 μm distance of each other. Barring one sample (#H2q/1: Association D) consisting of zoned garnet (Table 4), the compositions of minerals remain virtually constant within individual samples irrespective of the microdomains (i.e. biotite touching or separated by inert minerals such as quartz). This feature suggests that the kinetic barrier to Fe–Mg diffusion among the ferromagnesian minerals was minimal within the domains of chemical analyses.

The estimated temperature clusters within the range of 490 ± 40 °C (Table 8). The estimates yielded by the garnet–chlorite thermometry in the chloritoid–biotite schist in samples with the prefix #K3CG have not been considered within this cluster because the extreme Fe-rich composition of garnet in these samples is outside the composition range for which the garnet–chlorite thermometers are calibrated (Grambling 1990).

The estimated pressure values fall in narrow spreads of 6.78 ± 1.0 kbar (GBPQ) and 5.77 ± 0.90 kbar (GMPQ) (Table 8). A pressure of about 6.3 ± 1.1 kbar is obtained if all of the pressure estimates from the GBPQ and GMPQ barometers are combined. In view of the foregoing analyses, it is presumed that the metamorphism in the studied areas culminated at about 6.3 ± 1.1 kbar and

Table 3. *Representative analyses of biotite*

Association	A		B		C		D		E	
Sample no.	L5A/1	K3CG/1	K3/1	L5X/1	K5/1	G2/1	H2q/1	H2m/1	16A/1	16A/2
SiO_2	34.95	34.99	35.69	34.86	35.36	37.26	35.76	36.04	37.99	38.66
TiO_2	1.72	1.10	1.15	1.31	0.50	1.97	2.95	1.91	1.71	1.75
Al_2O_3	18.20	18.60	16.86	17.50	19.69	18.31	16.91	17.73	16.74	16.20
Cr_2O_3	0.02	0.10	0.01	0.00	0.02	0.07	0.08	0.05	0.03	0.00
FeO	23.10	23.49	24.36	22.93	22.22	18.44	20.88	19.94	19.33	20.15
MnO	0.02	0.10	0.00	0.04	0.02	0.01	0.01	0.06	0.20	0.12
MgO	7.40	7.82	7.28	8.96	8.30	10.86	8.53	9.61	9.71	9.45
CaO	0.02	0.00	0.01	0.04	0.10	0.16	0.06	0.10	0.40	0.45
Na_2O	0.17	0.01	0.14	0.20	0.42	0.11	0.09	0.13	0.09	0.09
K_2O	9.79	9.47	9.65	9.99	8.92	8.80	9.82	9.52	9.22	8.24
Total	95.40	95.68	95.15	95.83	95.55	95.99	95.09	95.08	95.42	95.11
Si	5.434	5.418	5.590	5.408	5.421	5.559	5.519	5.517	5.748	5.847
Ti	0.201	0.128	0.135	0.153	0.058	0.221	0.342	0.220	0.195	0.199
Al	3.336	3.395	3.113	3.201	3.559	3.221	3.077	3.199	2.986	2.889
Cr	0.002	0.012	0.001	0.000	0.002	0.008	0.010	0.006	0.004	0.000
Fe	3.004	3.042	3.191	2.975	2.849	2.301	2.695	2.553	2.446	2.549
Mn	0.003	0.013	0.000	0.005	0.003	0.001	0.001	0.008	0.026	0.015
Mg	1.715	1.805	1.699	2.072	1.897	2.415	1.962	2.192	2.190	2.130
Ca	0.003	0.000	0.002	0.007	0.016	0.026	0.010	0.017	0.065	0.073
Na	0.052	0.003	0.043	0.060	0.125	0.032	0.027	0.039	0.026	0.026
K	1.942	1.871	1.928	1.977	1.745	1.675	1.933	1.858	1.780	1.590
Cation total	15.692	15.687	15.703	15.857	15.675	15.459	15.576	15.609	15.465	15.318
X_{Mg}	0.363	0.372	0.347	0.410	0.400	0.512	0.421	0.462	0.472	0.455
End members (mol%)*										
Ti–biotite	10.06	6.40	6.77	7.64	2.88	11.06	17.12	10.98	9.73	9.95
Talc–minnesotite	0.32	6.31	1.46	0.00	6.52	14.66	1.98	5.14	9.69	19.18
Muscovite	7.91	7.10	8.97	6.05	8.88	5.54	6.26	6.75	9.65	8.77
Eastonite–siderophyllite	22.69	26.48	17.22	18.34	31.26	27.89	17.25	22.34	17.42	19.24
Wonesite	2.59	0.15	2.13	3.01	6.24	1.59	1.35	1.95	1.32	1.32
Phlogopite–annite	56.44	53.56	63.45	64.96	44.22	39.25	56.05	52.85	52.19	41.54

Note: *End-member recalculation after Holdaway *et al.* (1988); cation recalculation on 22(O).

Downloaded from http://sp.lyellcollection.org/ at Pennsylvania State University on September 16, 2016

Downloaded from http://sp.lyellcollection.org/ at Pennsylvania State University on September 16, 2016

Table 4. *Representative analyses of garnet*

Association	A				A	B				D				E	
Sample no.	L5A/2		K3CG/2		24C/1a	L5X/3		K3/1		H2 q/1		H2 q/2		16A/1	
	core	rim	core	rim		core	rim	core	rim	core	rim	core	rim	core	rim
SiO_2	37.01	36.91	35.81	36.24	36.26	35.86	35.66	36.84	37.02	37.96	36.50	36.48	37.21	35.82	35.79
TiO_2	0.05	0.03	0.00	0.04	0.01	0.00	0.00	0.01	0.00	0.14	0.06	0.00	0.04	0.07	0.01
Al_2O_3	21.08	21.09	20.90	20.94	20.43	21.30	21.14	20.93	21.09	21.78	21.66	20.74	20.73	20.62	20.84
Cr_2O_3	0.00	0.02	0.04	0.00	0.01	0.04	0.05	0.03	0.00	0.05	0.04	0.06	0.05	0.04	0.00
FeO	33.69	34.41	40.25	41.18	40.75	39.52	40.46	40.16	39.77	30.33	35.30	31.28	31.99	23.37	24.16
MnO	2.13	1.67	0.22	0.13	0.27	0.44	0.50	0.15	0.12	5.30	0.77	4.76	3.60	12.36	11.59
MgO	1.32	1.22	0.84	0.93	1.32	1.27	1.17	1.24	1.20	1.47	1.89	1.45	1.61	1.29	1.36
CaO	4.34	4.00	1.20	0.32	0.58	1.29	1.43	0.29	0.94	3.16	3.33	3.97	3.92	5.59	5.68
Na_2O	0.00	0.01	0.02	0.01	0.00	0.02	0.03	0.00	0.00	0.30	0.14	0.04	0.00	0.05	0.04
K_2O	0.00	0.02	0.02	0.00	0.01	0.00	0.00	0.00	0.00	0.00	0.00	0.00	0.00	0.00	0.00
Total	99.62	99.38	99.30	99.80	99.64	99.75	100.44	99.65	100.15	100.49	99.70	98.78	99.15	99.21	99.47
Si	6.003	6.006	5.925	5.963	5.977	5.888	5.849	6.030	6.023	6.056	5.914	5.982	6.050	5.879	5.858
Ti	0.006	0.004	0.000	0.005	0.001	0.000	0.000	0.001	0.000	0.017	0.008	0.000	0.005	0.009	0.001
Al	4.031	4.046	4.077	4.062	3.970	4.124	4.088	4.039	4.046	4.096	4.137	4.010	3.974	3.990	4.022
Cr	0.000	0.003	0.005	0.000	0.001	0.005	0.006	0.004	0.000	0.007	0.005	0.008	0.006	0.005	0.000
Fe^{2+}	4.569	4.682	5.570	5.667	5.589	5.426	5.550	5.497	5.412	4.047	4.782	4.290	4.330	3.203	3.307
Fe^{3+}*	0.000	0.000	0.000	0.000	0.028	0.000	0.000	0.000	0.000	0.000	0.000	0.000	0.020	0.005	0.000
Fe^{total}	4.569	4.682	5.570	5.667	5.618	5.426	5.550	5.497	5.412	4.047	4.782	4.290	4.350	3.208	3.307
Mn	0.293	0.230	0.031	0.018	0.038	0.062	0.069	0.021	0.017	0.716	0.106	0.661	0.496	1.718	1.607
Mg	0.318	0.296	0.207	0.228	0.324	0.311	0.286	0.304	0.292	0.349	0.457	0.354	0.390	0.316	0.332
Ca	0.754	0.697	0.213	0.057	0.102	0.227	0.251	0.050	0.164	0.540	0.577	0.698	0.683	0.983	0.996
Na	0.000	0.003	0.006	0.003	0.000	0.006	0.010	0.000	0.000	0.093	0.045	0.013	0.000	0.016	0.013
K	0.000	0.004	0.004	0.000	0.002	0.000	0.000	0.000	0.000	0.000	0.000	0.000	0.000	0.000	0.000
ΣCation	15.975	15.970	16.039	16.003	16.034	16.051	16.109	15.947	15.954	15.922	16.030	16.015	15.955	16.123	16.136
X_{Mg}	0.065	0.060	0.036	0.039	0.055	0.054	0.049	0.052	0.051	0.079	0.087	0.076	0.082	0.090	0.091
End members (mol%)															
Almandine	77.00	79.28	92.51	94.92	92.33	90.03	90.14	93.61	91.97	71.60	80.75	71.46	73.40	51.49	52.98
Pyrope	5.36	5.02	3.44	3.82	5.36	5.17	4.65	5.17	4.96	6.17	7.72	5.90	6.61	5.07	5.31
Grossular	12.70	11.81	3.53	0.95	1.69	3.77	4.08	0.85	2.78	9.56	9.75	11.62	11.58	15.81	15.96
Spessartine	4.94	3.89	0.51	0.31	0.62	1.03	1.13	0.36	0.29	12.67	1.79	11.01	8.40	27.63	25.74
Andradite	0.00	0.00	0.00	0.00	0.71	0.00	0.00	0.00	0.00	0.00	0.00	0.00	0.49	0.13	0.00

Note: *Fe^{3+} recalculation after Droop (1987) and cation recalculation on 24(O).

Downloaded from http://sp.lyellcollection.org/ at Pennsylvania State University on September 16, 2016

Table 5. *Representative chemical analyses of chlorite*

Association	A			C		D			
Sample no.	L5A/1	L5A/2	K3CG/2	K5/1	K5/2	H2q/2	H2q/3	G2/1	G2/2
SiO_2	22.99	22.83	22.75	22.76	22.98	23.84	25.19	23.83	23.66
TiO_2	0.08	0.13	0.33	0.11	0.02	0.24	0.10	0.07	0.09
Al_2O_3	21.51	22.03	22.49	22.50	23.38	21.94	21.61	22.21	21.84
Cr_2O_3	0.02	0.01	0.00	0.05	0.05	0.02	0.04	0.09	0.04
FeO	30.16	29.73	30.33	29.34	29.50	28.25	25.07	27.88	27.47
MnO	0.06	0.05	0.29	0.08	0.11	0.12	0.20	0.04	0.01
MgO	9.49	9.59	9.68	10.57	9.56	11.11	12.74	12.35	12.25
CaO	0.08	0.02	0.00	0.15	0.08	0.14	0.13	0.01	0.01
Na_2O	0.08	0.04	0.44	0.14	0.12	0.15	0.17	0.01	0.01
K_2O	0.11	0.03	0.02	0.01	0.01	0.12	0.22	0.01	0.00
Total	84.58	84.47	86.33	85.72	85.81	85.93	85.46	86.50	85.38
Si	5.183	5.138	5.021	5.020	5.062	5.212	5.431	5.166	5.191
Ti	0.014	0.022	0.055	0.018	0.003	0.040	0.016	0.011	0.015
Al	5.717	5.845	5.851	5.852	6.073	5.655	5.493	5.676	5.649
Cr	0.004	0.002	0.000	0.009	0.008	0.003	0.007	0.015	0.007
Fe^{2+}	5.508	5.453	5.306	5.212	5.283	4.923	4.300	4.951	4.934
Fe^{3+}*	0.177	0.142	0.288	0.198	0.151	0.241	0.219	0.103	0.105
Fe^{total}	5.685	5.594	5.594	5.410	5.435	5.164	4.519	5.054	5.039
Mn	0.011	0.010	0.055	0.015	0.021	0.023	0.036	0.007	0.002
Mg	3.189	3.217	3.182	3.474	3.140	3.621	4.094	3.990	4.006
Ca	0.019	0.005	0.000	0.036	0.020	0.034	0.030	0.002	0.002
Na	0.035	0.018	0.188	0.060	0.050	0.062	0.071	0.004	0.004
K	0.032	0.009	0.006	0.003	0.003	0.033	0.060	0.003	0.000
Σcation	19.888	19.859	19.951	19.897	19.815	19.846	19.758	19.929	19.916
X_{Mg}	0.367	0.371	0.375	0.400	0.373	0.424	0.488	0.446	0.448

Note: *Fe^{3+} recalculation after Zane *et al.* (1998), $X_{Mg} = Mg/(Mg + Fe^{2+})$; cation calculation on 28(O).

490 ± 40 °C. The presence of kyanite in the adjoining kyanite–quartzite and kyanite–mica schist is consistent with the inferred *P–T* values for the peak metamorphism in the studied areas.

Mineral reactions in chloritoid–biotite schist

In the absence of definitive mineral inclusion, mineral reactions that stabilized chloritoid in the studied rocks remain unclear. Nevertheless, the following KFMASH (K_2O–FeO–MgO–Al_2O_3–SiO_2–H_2O) model reaction seems to be a distinct possibility:

$$Ms + Chl \longrightarrow Cld + Bt + Qtz + H_2O. \quad (1)$$

For chlorite-free rock, textural relations described before are consistent with the KFMASH reaction,

$$Cld + Bt + Qtz \longrightarrow Grt + Ms + H_2O. \quad (2)$$

Reactions (1) and (2) are consistent with the chemographical projections in the AFM plane (Fig. 5a, b).

Textural features demonstrate that garnet and chlorite were developed after the formation of biotite and chloritoid (Figs 3d, f & 4a–d), which by implication suggests following tie-line switching reaction involving the AFM phases in the system KFMASH (Fig. 5c):

$$Cld + Bt \longrightarrow Grt + Chl. \quad (3)$$

H_2O is always placed on the right-hand side of reaction (3) – that is, with garnet + chlorite – except in the balanced reaction given by Labotka 1980 (Table 9). Mineral compositions of #K3CG/1 have been used to balance the reaction as non-KFMASH components are minimal in the rock (Table 9). Ignoring the small concentrations of the non-KFMASH components, the balanced reaction places H_2O on the same side as garnet and chlorite:

$$10.58Cld + 4.81Bt + 9.21Qtz = 3.97Grt + 2.40Chl + 4.81Ms + H_2O. \quad (3)$$

The implication of this reaction is discussed in the following section.

Downloaded from http://sp.lyellcollection.org/ at Pennsylvania State University on September 16, 2016

Table 6. *Representative analyses of muscovite*

Association	A				B			C	D				E	
Sample no.	L5A/1	L5A/2	K3CG/1	K3CG/1	L5X/1	K3/1	K3/2	K5/2	G2/1	G2/4	H2q/1	H2m/1	16A/1	16A/1
SiO_2	47.82	48.02	46.86	47.26	46.54	47.93	47.51	46.71	47.43	47.37	47.33	46.85	47.66	46.89
TiO_2	0.27	0.28	0.08	0.24	0.28	0.41	0.24	0.03	0.20	0.24	0.30	0.55	0.54	0.70
Al_2O_3	34.16	33.93	35.35	34.26	35.34	33.00	33.62	35.57	34.25	34.22	34.62	33.94	32.10	31.90
Cr_2O_3	0.02	0.00	0.06	0.02	0.04	0.02	0.04	0.02	0.02	0.00	0.06	0.06	0.05	0.00
FeO	2.32	2.41	1.76	2.77	3.22	3.02	2.94	2.34	2.95	2.50	2.32	2.69	4.44	4.46
MnO	0.03	0.02	0.04	0.00	0.00	0.07	0.03	0.07	0.05	0.01	0.01	0.04	0.04	0.03
MgO	0.73	0.67	0.92	0.74	0.80	1.16	0.93	0.70	0.68	1.23	0.96	0.99	1.24	1.18
CaO	0.03	0.00	0.03	0.02	0.01	0.03	0.02	0.04	0.19	0.03	0.01	0.09	0.02	0.04
Na_2O	0.79	0.80	0.50	0.47	0.54	0.57	0.53	0.50	1.06	1.28	1.20	1.02	0.41	0.57
K_2O	10.49	10.51	10.49	10.40	9.69	10.08	10.16	10.18	9.04	9.26	9.46	9.86	9.25	10.19
Total	96.66	96.64	96.09	96.18	96.46	96.29	96.02	96.16	95.87	96.14	96.27	96.09	95.75	95.96
Si	6.299	6.327	6.191	6.263	6.144	6.345	6.305	6.173	6.276	6.251	6.235	6.218	6.360	6.296
Ti	0.027	0.028	0.008	0.024	0.028	0.041	0.024	0.003	0.020	0.024	0.030	0.055	0.054	0.071
Al	5.305	5.270	5.506	5.352	5.500	5.150	5.260	5.542	5.343	5.323	5.377	5.311	5.050	5.049
Cr	0.002	0.000	0.006	0.002	0.004	0.002	0.004	0.002	0.002	0.000	0.006	0.006	0.005	0.000
Fe	0.256	0.266	0.195	0.307	0.356	0.334	0.326	0.259	0.326	0.276	0.256	0.299	0.495	0.501
Mn	0.003	0.002	0.004	0.000	0.000	0.008	0.003	0.008	0.006	0.001	0.001	0.004	0.005	0.003
Mg	0.143	0.132	0.180	0.146	0.157	0.229	0.184	0.138	0.134	0.242	0.188	0.196	0.247	0.236
Ca	0.004	0.000	0.004	0.003	0.001	0.004	0.003	0.006	0.027	0.004	0.001	0.013	0.003	0.006
Na	0.202	0.204	0.129	0.121	0.138	0.146	0.136	0.128	0.272	0.327	0.307	0.263	0.106	0.148
K	1.763	1.767	1.769	1.758	1.632	1.702	1.720	1.716	1.526	1.559	1.590	1.670	1.575	1.746
Σcation	14.003	13.996	13.993	13.976	13.961	13.962	13.967	13.974	13.931	14.007	13.992	14.034	13.899	14.056
End members (mol%)*														
Ti–muscovite	1.34	1.39	0.40	1.20	1.39	2.04	1.20	0.15	1.00	1.19	1.49	2.75	2.71	3.53
Phlogopite–annite	1.46	1.11	4.03	4.59	9.26	4.97	4.99	5.71	4.93	5.77	4.31	3.93	10.28	7.64
Celadonite	14.24	15.13	6.26	7.68	0.00	11.21	9.35	2.54	7.24	7.38	7.79	10.20	3.55	10.40
Pyrophyllite	1.24	1.34	4.20	5.75	9.35	6.80	6.54	6.94	8.32	5.41	4.58	2.06	15.20	4.85
Paragonite	10.09	10.22	6.45	6.04	6.91	7.32	6.82	6.41	13.60	16.37	15.33	13.13	5.30	7.42
Margarite	0.21	0.00	0.21	0.14	0.07	0.21	0.14	0.28	1.35	0.21	0.07	0.64	0.14	0.29
Muscovite	71.43	70.82	78.44	74.60	73.03	67.45	70.96	77.97	63.57	63.66	66.44	67.31	62.82	65.88

Note: *End-member recalculation after Holdaway *et al.* (1988); cation recalculation on 22(O).

Table 7. *Representative analyses of plagioclase (Pl) and ilmenite (Ilm)*

Mineral	Pl						Ilm					
Association	D				C		A		B	D		E
Sample no.	G2/1	G2/2	H2q/1	H2q/2	16A/1	16A/2	L5A/1	24C/1 (incl-Cld)	K3/1 (incl-Grt)	G2/1	H2q/1	16A/1
SiO_2	62.16	61.59	62.94	62.26	62.98	62.50	0.02	0.04	0.04	0.13	0.03	0.05
TiO_2	0.00	0.00	0.00	0.02	0.00	0.00	54.00	55.67	52.23	54.74	52.81	53.94
Al_2O_3	23.51	23.90	23.41	23.63	23.31	24.11	0.00	0.05	0.05	0.01	0.00	0.04
Cr_2O_3	0.03	0.02	0.00	0.00	0.00	0.00	0.01	0.06	0.05	0.05	0.06	0.00
FeO	0.15	0.19	0.36	0.08	0.10	0.07	44.97	43.92	47.05	44.24	45.08	41.82
MnO	0.00	0.02	0.00	0.00	0.04	0.00	0.31	0.06	0.05	0.40	1.39	3.81
MgO	0.00	0.00	0.00	0.01	0.00	0.00	0.06	0.13	0.19	0.10	0.01	0.00
CaO	4.22	5.20	4.75	4.84	4.53	5.71	0.01	0.00	0.01	0.00	0.02	0.00
Na_2O	9.92	9.24	9.13	8.90	8.81	7.65	0.04	0.02	0.15	0.02	0.01	0.02
K_2O	0.06	0.05	0.05	0.11	0.07	0.06	0.06	0.00	0.00	0.00	0.01	0.11
Total	100.05	100.21	100.64	99.85	99.84	100.10	99.49	99.96	99.82	99.68	99.43	99.80
Si	2.759	2.734	2.773	2.762	2.788	2.758	0.001	0.001	0.001	0.003	0.001	0.001
Ti	0.000	0.000	0.000	0.001	0.000	0.000	1.021	1.038	0.993	1.028	1.005	1.018
Al	1.230	1.251	1.216	1.236	1.216	1.254	0.000	0.002	0.001	0.000	0.000	0.001
Cr	0.001	0.001	0.000	0.000	0.000	0.000	0.000	0.001	0.001	0.001	0.001	0.000
Fe	0.006	0.007	0.013	0.003	0.004	0.003	0.946	0.911	0.995	0.924	0.954	0.877
Mn	0.000	0.001	0.000	0.000	0.001	0.000	0.007	0.001	0.001	0.008	0.030	0.081
Mg	0.000	0.000	0.000	0.001	0.000	0.000	0.002	0.005	0.007	0.004	0.000	0.000
Ca	0.201	0.247	0.224	0.230	0.215	0.270	0.000	0.000	0.000	0.000	0.001	0.000
Na	0.854	0.795	0.780	0.766	0.756	0.655	0.002	0.001	0.007	0.001	0.001	0.001
K	0.003	0.003	0.003	0.006	0.004	0.003	0.002	0.000	0.000	0.000	0.000	0.004
Σcation	5.054	5.039	5.010	5.005	4.984	4.943	1.980	1.960	2.008	1.969	1.994	1.983
X_{Ab}	0.810	0.763	0.777	0.769	0.779	0.708						
X_{An}	0.190	0.237	0.223	0.231	0.221	0.292						

Note: Cation recalculation of Pl and Ilm, respectively, on 8(O) and 3(O); incl: included within porphyroblast.

Downloaded from http://sp.lyellcollection.org/ at Pennsylvania State University on September 16, 2016

Downloaded from http://sp.lyellcollection.org/ at Pennsylvania State University on September 16, 2016

Table 8. *Temperature (°C) and pressure (kbar) estimated from representative mineral compositions*

Sample no.*	Analysis no.	T^1 (°C)	T^2 (°C)	T^3 (°C)	T^4 (°C)	T^5 (°C)	T^6 (°C)	T^7 (°C)	Sample no.†	Analysis no.	T^1 (°C)	T^2 (°C)	T^3 (°C)	T^4 (°C)	T^5 (°C)	T^6 (°C)	T^7 (°C)	P^1 (kbar)	P^2 (kbar)
L5A/1	1 rim	510	511	530	506	484	489	480	H2 q/1	1 rim	514	522	530	506	466	474	464	7.51	4.98
	1 core	530	516	542	517	519	514	509		1 core	458	460	490	482	435	448	438	6.04	3.44
L5A/2	1 rim	498	514	533	503	487	491	482	H2 q/3	2 rim	502	513	522	558	533	524	521	7.90	5.90
	1 core	514	516	540	513	509	507	501		2 core	476	480	503	552	530	522	519	5.11	6.53
K3CG/1	1 rim	472	488	475	495	408	423	415	H2 q/4	1 rim	494	490	534	530	518	514	508	7.51	6.26
	1 core	482	495	488	487	389	405	399		1 core	452	463	490	509	490	493	485	5.93	5.84
K3CG/2	1 rim	455	477	480	481	417	432	422	H2 q/5	3 rim	483	490	510	519	511	509	503	7.26	4.09
	1 core	474	489	497	484	424	438	428		3 core	440	453	485	496	461	470	460	4.72	6.47
K3CG/3	2 rim	459	483	486	470	391	407	400	H2m/1	1 rim	554	538	593	546	548	534	533	7.90	6.53
	2 core	506	509	513	502	426	440	430		1 core	501	513	558	513	463	472	462	7.92	7.01
24C/1	1 rim	478	490	488	490	439	452	442	H2m/2	4 rim	531	536	588	542	525	519	514	7.67	6.43
	1 core	500	506	503	503	471	478	469		4 core	453	470	530	498	389	405	399	6.49	5.96
24C/1a	2 rim	482	493	488	474	453	464	454	G2/1	1 rim	487	495	516	479	480	475	508	6.46	6.49
	2 core	494	502	493	479	459	469	459		1 core	482	490	518	476	493	496	488	6.47	6.31
L5X/1	1 rim	443	468	468	500				G2/1a	2 rim	480	475	503	475	492	495	486	5.09	5.89
	1 core	449	475	476	505					2 core	485	480	510	480	480	465	490	5.26	6.04
L5X/2	1 rim	428	459	455	477				G2/3	2 rim	487	492	513	465	500	470	478	5.77	6.01
	1 core	417	450	444	470					2 core	483	490	512	463	496	470	475	5.96	6.00
L5X/3	2 rim	413	448	445	489				G2/5	4 rim	475	486	498	470	465	474	464	6.53	4.97
	2 core	427	462	460	499					4 core	498	512	522	485	472	480	465	6.27	3.77
K3/1	1 rim	462	482	477	446				16A/1	1 rim	463	475	495	495				7.37	5.33
	1 core	481	496	494	457					1 core	464	479	472	484				7.18	5.66
K3/2	2 rim	466	485	475	474				16A/2	2 rim	469	480	480	487				7.98	6.59
	2 core	479	495	490	480					2 core	461	470	476	489				8.46	6.09
K3/3	1 rim	456	472	474	469				16A/4	1 rim	469	480	477	527				7.56	5.66
	1 core	490	498	491	470					1core	469	480	492	527				7.37	5.67
Average		472	488	489	486	448	458	449			482	489	512	502	487	485	483	6.76	5.77
Standard deviation		30	20	26	18	42	35	36			25	22	31	28	37	30	32	1.05	0.88

Note: *Chloritoid–biotite schist; †Psammopelitic schist; T^{1-3}, Grt–Bt thermometers; T^1, Ganguly & Saxena (1984); T^2, Perchuk & Lavrentieva (1983); T^3, Holdaway (2000); T^4, Grt–Ms thermometer (Hynes & Forest 1988); T^{5-7}, Grt–Chl thermometers; T^5, Dickenson & Hewitt (1986); T^6, Grambling (1990); T^7, Ghent *et al.* (1987); P^1, Grt–Bt–Pl–Qtz barometer (Wu *et al.* 2004); P^2, Grt–Ms–Pl–Qtz barometer (Wu & Zhao 2006).

Downloaded from http://sp.lyellcollection.org/ at Pennsylvania State University on September 16, 2016

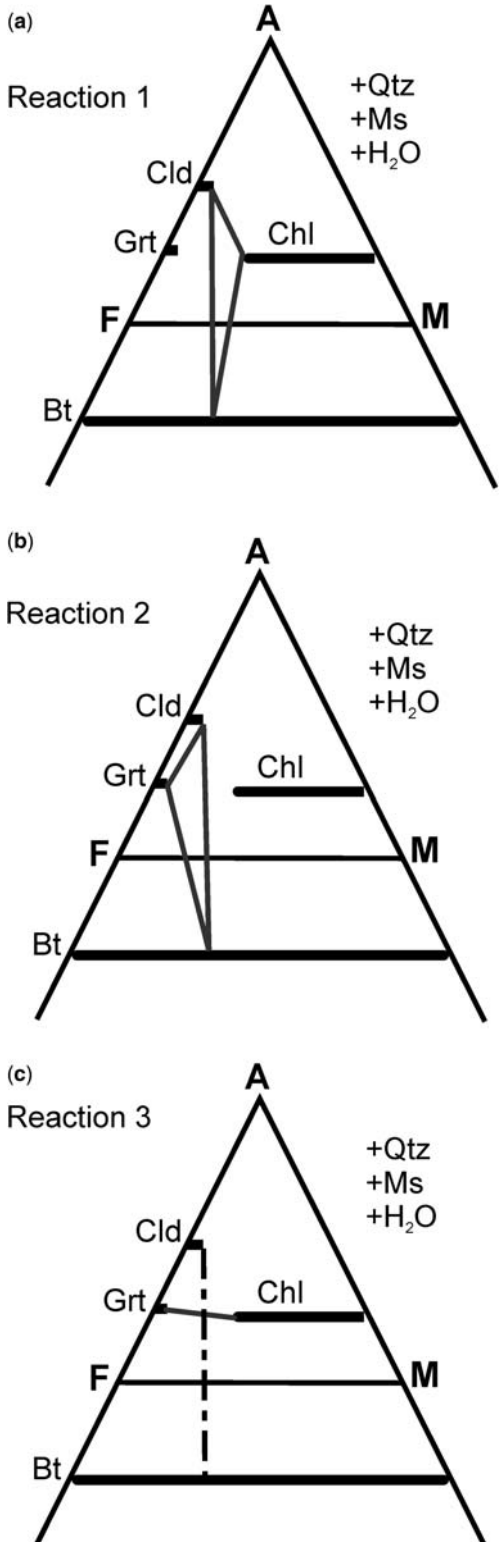

Stability of chloritoid + biotite v. garnet + chlorite

Petrogenetic grid in the KFMASH system

In the six-component KFMASH system, the phases garnet–chloritoid–aluminosilicates–staurolite–biotite–chlorite–quartz–muscovite–H_2O ($P = 9$) has a variance of -1. If the three minerals – namely, quartz, muscovite and H_2O – are considered to be omnipresent, there will be a maximum of six invariant points [Cld], [Grt], [Als], [St], [Bt] and [Chl]. The mineral assemblages of the univariant reactions related to the [Als] invariant point are widespread in medium-grade metapelites. Therefore, understanding the topological relations around this invariant point is crucial in interpreting the observed mineralogy and their mutual relations in the low- to medium-grade metapelites. Different workers suggested contrasting topological phase relations around the [Als] invariant point (Albee 1965; Harte & Hudson 1979; Labotka 1981; Spear & Cheney 1989; Powell & Holland 1990; Wang & Spear 1991; Droop & Harte 1995). The nature and orientation of the (Als, St) univariant reaction that involves the four AFM phases garnet, chlorite, chloritoid and biotite is the main source of dispute between different workers.

The published topology can be divided into two basic types. Figure 6 describes the contrasting topological relations around the [Als] invariant point. The topology presented in Figure 6a was initially proposed by Albee (1965, 1972) from the reaction textures of a suite of metapelites, and was subsequently supported by Harte & Hudson (1979) and Droop & Harte (1995). In this topological arrangement, the univariant reaction (Als, St) has a positive slope, and the restricted P–T stability field with chloritoid + biotite is placed on the low-pressure side of the reaction (Als, St) below the [Als] invariant point (*c*. 6 kbar, Fig. 6a). The internally consistent thermodynamic database of Powell & Holland (1990) does not stabilize the [Als] invariant point in the KFMASH system. However, if Fe_2O_3 is incorporated into this system, the [Als] invariant point stabilizes and the observed topological relations are similar to that of Harte & Hudson (1979) and Droop & Harte (1995).

Using the internally consistent thermodynamic database, Spear & Cheney (1989) proposed a drastically different topology around the [Als] invariant

Fig. 5. Chemographic projections of the silicate phases representing different mineral reactions in chloritoid–biotite schist: (**a**) Ms + Chl → Cld + Bt + Qtz + H_2O − (1); (**b**) Cld + Bt + Qtz → Grt + Ms + H_2O − (2); and (**c**) Cld + Bt + Qtz → Grt + Chl + Ms + H_2O − (3).

Downloaded from http://sp.lyellcollection.org/ at Pennsylvania State University on September 16, 2016

Table 9. *Balanced (Als, St) KFMASH reactions deduced from the chemical composition of the mineral phases in different areas*

Area	Balanced reaction	Source
South Brittany, France	$10Bt + 23.8Cld + 17.85Qtz = 8.6Grt + 2.73Chl + 10Ms + 1.96H_2O$	Triboulet (1983)
Tri-state, USA	$1.82Bt + 4.04Cld + 10Qtz = 2.85Grt + 0.70Chl + 3.43Ms + 0.88H_2O$	Wang & Spear (1991)
Tauern Window	(i) $1.71Bt + 4.40Cld + 3.8Qtz = 1.9Grt + Chl + 1.71Ms + 0.40H_2O$ (ii) $1.56Bt + 4.20Cld + 3.88Qtz = 1.86Grt + Chl + 1.56Ms + 0.20H_2O$	Droop & Harte (1995)
Vermont, USA	$1.32Bt + 5.21Cld + 3.95Qtz = 1.39Grt + Chl + 1.32Ms + 1.21H_2O$	Albee (1965)
Funeral Mt, California	$1.63Bt + 1.79Cld + 2.88Qtz + 0.42H_2O = 1.11Grt + Chl + 1.63Ms$	Labotka (1980)
Kanyaluka, SSZ	$4.81Bt + 10.58Cld + 9.21Qtz = 3.97Grt + 2.40Chl + 4.81Ms + H_2O$	Present study

point (Fig. 6b). They showed that because of the strong and opposite curvature of the univariant reactions (Als, St) and (Als, Cld), two [Als] invariant points stabilize, one at high pressure (14.8 kbar, 580 °C) and another at low pressure (6.5 kbar, 545 °C). An important feature of this grid is that the (Als, St) reaction is relatively insensitive to pressure and the garnet + chlorite is stabilized at a higher temperature compared to chloritoid + biotite (Fig. 6b).

In favour of the topological relationships proposed by the Spear & Cheney (1989) topology around the [Als] invariant point, Wang & Spear (1991) presented the following arguments.

- The appearance of chloritoid + biotite in metapelites at pressures as high as 7 kbar in SE Tauern Window, Austria can be explained using the grid of Spear & Chenny (1989), but is inconsistent with the grid proposed by Harte & Hudson (1979). This is because the latter allows only low-pressure (<6 kbar) stability of the chloritoid + biotite-bearing assemblage in the system KFMASH.
- The mass-balance calculations by least-squares method using the phases of the reaction (Als, St) in the Mn–Ca–Na-poor rocks show H_2O to be present with garnet + chlorite in most places (Table 9). This is consistent with higher entropy and, therefore, high-temperature stability of garnet + chlorite compared to chloritoid + biotite.
- The textural features and the phase compositional attributes of the four-phase assemblages (garnet–chlorite–chloritoid–biotite) from a Barrovian sequence of a tri-state area in the

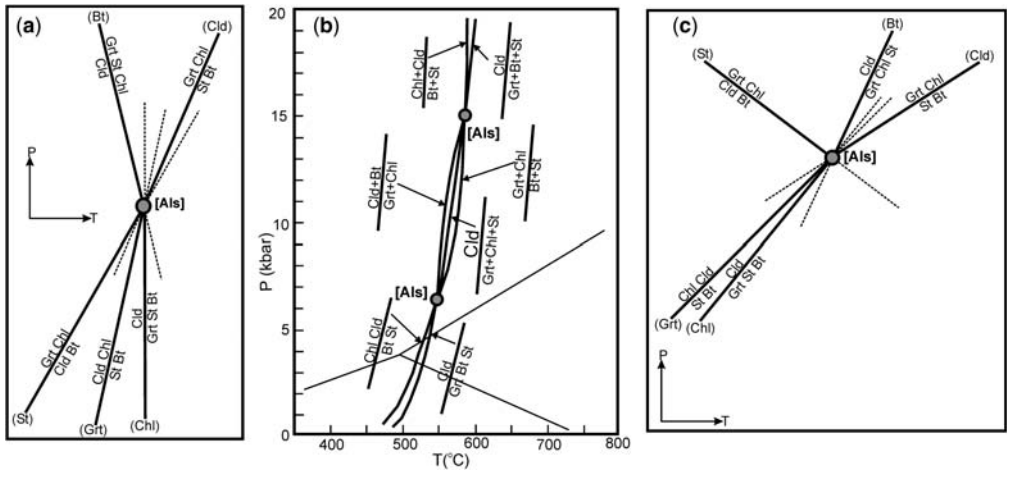

Fig. 6. Geometrical arrangements of the univariant reactions around the aluminosilicate-absent [Als] invariant point in the system KFMASH. (**a**) Wang & Spear (1991), (**b**) Harte & Hudson (1979) and (**c**) present study. Note that the arrangements depicted in both (b) and (c) are similar, and both satisfy the Schreinemakers' principals.

Downloaded from http://sp.lyellcollection.org/ at Pennsylvania State University on September 16, 2016

Taconic Range (Wang & Spear 1991) show the low-temperature stability of chloritoid + biotite compared to garnet + chlorite in Mn-poor rocks. This is consistent with the topology presented by Spear & Cheney (1989) but inconsistent with that of Harte & Hudson (1979) (Fig. 6a, b). However, the enlarged stability field of garnet + chlorite for the Mn-rich bulk composition explains the stability of garnet + chlorite at lower temperature rather than that of chloritoid + biotite (Wang & Spear 1991). The enlargement of the stability field of garnet-bearing assemblages was first demonstrated by Ganguly (1968), which was further substantiated by Loomis (1986)

In support of the topological relation of Harte & Hudson (1979), Droop & Harte (1995) presented the following arguments.

- In most of the natural rocks, chloritoid + biotite are found to stabilize at or below 7 kbar pressure. At higher pressures, garnet + chlorite are the dominant minerals at temperature below the staurolite-in isograd. This is consistent with the topology of Harte & Hudson (1979), which predicts stability of chloritoid + biotite below $P[_{Als}]$ of around 7 kbar, but is inconsistent with the arrangements proposed by Spear & Cheney (1989), which predicts chloritoid + biotite to occur over a large range of pressures (Fig. 6b).
- Where present, the zone containing the garnet + chlorite zone is generally found to develop at lower grade relative to zones with chloritoid + biotite. This observation can be readily explained by the geometrical arrangements of Harte & Hudson (1979) but not by those of Spear & Cheney (1989). Furthermore, Droop & Harte (1995) cited the crucial observation of Labotka (1980) to contradict Wang & Spear (1991). Labotka (1980) described a garnet + chlorite assemblage close to the garnet-in isograd in Mn-poor metapelites from the Funeral Mountain, California, where garnet + chlorite assemblage gave away directly to staurolite-bearing assemblages without any intermediate chloritoid + biotite zone.
- The chloritoid + biotite zone is generally absent from the typical Barrovian sequences. When present, chloritoid + biotite-bearing assemblages develop only in aluminous rocks that plot in the high-Al side of the critical garnet–chlorite join in AFM plots (Droop & Harte 1995). This observation is inconsistent with the arrangements presented by Spear & Cheney (1989) because this topological arrangement cannot explain any bulk compositional restriction for the stability of chloritoid + biotite in low-grade metapelites.

A careful scrutiny of the published literature reveals the following points.

- Table 9 presents the stoichiometrically balanced reaction involving Cld, Bt, Grt and Chl in rocks with bulk compositions effectively represented by the KFMASH system. It is clear from Table 9 that H_2O, in most places, coexists with garnet + chlorite, which suggests that chloritoid + biotite is present in the lower temperature of the reaction. This feature is in agreement with the topology of Spear & Chenny (1989). But in the reaction provided by Labotka (1980), H_2O is placed with chloritoid + biotite. A careful scrutiny of his data reveals that these four phases never coexist in one sample. It is, therefore, not clear whether the compositions of minerals used to balance the reaction are of equilibrium assemblage or not.
- Table 10 presents the P–T conditions of metamorphism and composition of garnet (if present) in low- to medium-grade metapelites containing chloritoid + biotite. It is evident from Table 10 that chloritoid + biotite-bearing assemblages do not occur at pressures much above 7 kbar. This feature is corroborated by the topology of Droop & Harte (1995).
- Natural examples presented in Table 10 demonstrate that garnet + chlorite appears early in a progressive metamorphic sequence, only when the bulk composition of the rock is rich in Ca and Mn (reflected in the garnet composition). This is consistent with the observation of Wang & Spear (1991). However, the absence of chloritoid + biotite in one Ca–Mn-poor metapelite occurrence described by Labotka (1981) merits discussion at this stage. From the muscovite + plagioclase-bearing assemblages, Labotka (1981) calculated a range of X_{H_2O} values (0.32–0.83) for pelitic rocks, which indicates a significant dilution of H_2O by non-hydrous fluid species. If the concentration of H_2O is diluted, then garnet + chlorite will be preferred over chloritoid + biotite, as H_2O is present with garnet + chlorite in the stoichiometrically balanced reaction (Table 9). This possibly explains the non-appearance of chloritoid + biotite in the Ca–Mn-poor and andalusite-bearing rocks of Paramint Mountain, California (Labotka 1981). This then follows that garnet + chlorite will develop prior to chloritoid + biotite if the rock is rich in Ca and Mn, and/or equilibrates with fluids other than pure H_2O. This contention is supported by stability of chloritoid + biotite in the Ca–Mn-poor metapelites and the absence of this assemblage in the Ca–Mn-rich psammopelites of the SSZ.

Downloaded from http://sp.lyellcollection.org/ at Pennsylvania State University on September 16, 2016

Table 10. *The occurrence of the assemblage Cld + Bt + Grt + Chl*

Locality	Stable Al-silicate	Garnet $X_{Ca} + X_{Mn}$	P (kbar)	T (°C)	Source	Remarks
Dalradian, Scotland	–	–	*c.* 7.5	550–600	Baltatzis & Wood (1977)	+Ab ±Pg
Naxos, Greece*	Ky, Sill	–	7–9	490–530	Andriessen *et al.* (1979)	+Gln +Ep +Ab +Pg, no Grt
South Brittany, France	–	0.22	6 ± 0.5	500–540	Triboulet (1983)	
Hida terrane, Central Japan	–	0.16–0.18	5	540	Hiroi (1983)	+St
Yilgarn Block, Australia	And	0.07–0.16	4.2	530–560	Bickle & Archibald (1984)	+St ±Crd ±And ±Pl
Mt Moosilauke, New Hampshire, USA	And	0.08	3.5–4	520	Dickenson (1988)	
Eastern Rhodope Zone, northern Greece	Sill	0.09	11	550	Mposkos (1989)	+St +Pg
Truchas Range, New Mexico, USA	Ky, And, Sill	0.06	4	500–550	Grambling (1983)	+St +Rt
Tri-state, USA	Ky	0.03	4.4–4.8	490–530	Wang & Spear (1991)	
Stonehaven, Scotland	–	–	*c.* 5	500 ± 25	Droop & Harte (1995)	
SE Tauern Window, Austria	Ky	0.15–0.22	7 ± 1	475 ± 25	Droop & Harte (1995)	
Dutches County, NY, USA	Ky	0.17	4	475–480	Whitney *et al.* (1996)	+Pl
Hlinsko region, Bohemian massif, Czech Republic	And	0.22–0.28	4	530–570	Pitra & Guiraud (1996)	+St +And
Island of Kos, Greece*	–	0.03	2	600	Kalt *et al.* (1998)	+Crd +St +Pl, no Chl
Moldanubicum, Bohemian massif, Czech Republic*	And	–	4.2 ± 1.9	<500	Babûrek (1998)	No Chl and Grt
Ayakhtinsk aureole, Siberia*	And		3.2 ± 0.3	450	Likhanov *et al.* (2001)	No Chl and Grt
Mungyong coalfield, central South Korea*	And	–	1–2	–	Ahn & Nakamura (2000)	+And, no Grt
Bushveld Complex, South Africa*	And	–	3.5	<450	Waters & Lovegrove (2002)	+St +Crd, no Grt
The SSZ, eastern India	Ky	0.01–0.17	6.5 ± 0.5	480 ± 40	Present study	

Note: *Indicates the absence of chlorite and/or garnet; the localities written in bold font record the assemblage stable without staurolite.

Downloaded from http://sp.lyellcollection.org/ at Pennsylvania State University on September 16, 2016

It is, therefore, evident from the foregoing analyses that none of the existing grids can explain all of the following features:

- the restriction of chloritoid + biotite at pressures below 7 kbar;
- the formation of chloritoid + biotite prior to garnet + chlorite in Ca–Mn-poor rocks of the studied area;
- the occurrence of H_2O on the same side as garnet + chlorite in #K3CG/1 where the concentration of non-KFMASH components are minimal.

With this backdrop, a new petrogenetic grid in parts of the KFMASH system has been developed integrating the extant petrological, phase chemical and experimental data (Figs 6c & 7). In this grid, the KFASH invariant point [Bt, Chl] has been considered to be stable together with [Bt, Grt], [Cld, Grt], [Cld, Chl], [Grt, Als] and [Chl, Als]. Slopes of most of the univariant KFASH reactions are taken from the experimental data of Ganguly (1972), and from Harte & Hudson (1979) and Spear & Cheney (1989) (Fig. 7). The slopes of the rest (marked with a star in Fig. 7) have been construed from mutual topological relationships with the other reactions. Owing to the large uncertainties of the thermodynamic data of the phases, the KFMASH topology was derived from the KFASH reaction nets following Schreinemaker's principals (Fig. 7). This approach stabilized three KFMASH invariant points namely, [Cld], [St] and [Bt]. The controversial univariant reaction (Als, St) assumes a moderate negative slope with chloritoid + biotite on the low-pressure side (Figs 6c & 7). Weak to strong negative P–T slope is not uncommon for dehydration reactions above about 5 kbar (fig. 3 of Ganguly 1972; fig. 9.12 of Spear 1993).

Barring the slopes of the KFMASH univariant reactions (Als, St) and (Als, Bt), topology of the proposed grid is in agreement with the topology predicted by Harte & Hudson (1979) (Fig. 6a). Both the topologies are, however, correct on the basis of Schreinemaker's principals. The new grid depicted in Figure 7 can explain: (a) the restriction of chloritoid + biotite at lower pressures and

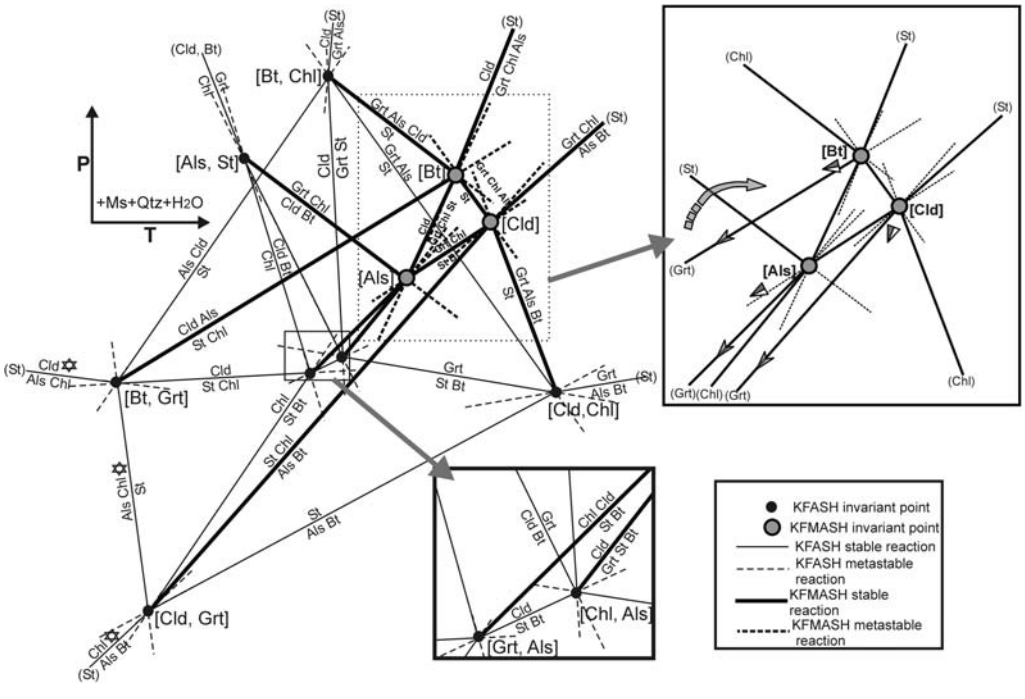

Fig. 7. Schematic partial petrogenetic grid in the KFASH (thin line) and KFMASH (thick lines) systems involving garnet, staurolite, chloritoid, biotite, chlorite, muscovite, aluminosilicate, quartz and H_2O. Note that the (Als, St) reaction has a negative slope with chloritoid + biotite on the low–P, low–T side of the reaction. The inset in the NE corner of the figure shows the likely P–T path of the studied rocks. The arrowheads depict the direction along which the KFMASH invariant points will shift due to the addition of Mn (filled arrowhead) and the reduced activity of H_2O (half-filled arrowhead).

Downloaded from http://sp.lyellcollection.org/ at Pennsylvania State University on September 16, 2016

temperatures compared to garnet + chlorite; and (b) the formation of garnet + chlorite from chloritoid + biotite during the progressive metamorphism of Mn-poor metapelites, as is documented in this study. Garnet is a strong sink for Mn (and also for Ca). Therefore, in Mn-rich metapelite, the KFMASH invariant points [Cld], [Als] and [Bt] will be displaced towards lower P–T conditions along their corresponding garnet-absent univariant reactions (Fig. 7). The effect of the reduction of H_2O will be the same as the effect of Mn in bulk rock composition (Fig. 7). The net effect of an increase in Mn and a reduction of H_2O will be to reduce the P–T field of chloritoid + biotite and to restrict the assemblage at very low pressure (Fig. 7). This probably explains the rarity of the chloritoid + biotite and preponderance of garnet + chlorite in low- to medium-grade metapelites. The influences of the non-KFMASH components also explain the early development of chloritoid + biotite in Mn–Ca-poor metapelite and garnet + chlorite in Mn–Ca-rich psammopelitic schist in the SSZ.

Pseudosections in parts of the Na_2O–CaO–MnO–K_2O–FeO–MgO–Al_2O_3–SiO_2–H_2O–O (NCMnKFMASHO) system

With the availability of an internally consistent thermodynamic dataset and the activity–composition relationships of solid-solution phases, it is now possible to compute phase diagrams numerically that portray mineralogical changes in a given bulk composition in response to the changing pressure, temperature and chemical potentials of H_2O and O_2. For this purpose, the computer program PERPLE_X 07 (Connolly 2005) is used along with the internally consistent thermodynamic dataset of Holland & Powell (1998, updated in 2004). Activity–composition relationships used for different solid-solution phases are: garnet (Ganguly *et al.* 1996), staurolite (Holland & Powell 1998), chlorite (Holland *et al.* 1998), biotite and muscovite (Powell & Holland 1999), and plagioclase (Newton *et al.* 1980). Use of the garnet solution model of Holland & Powell (1998) does not change the topology of the calculated phase diagrams.

Considering the bulk compositions and the mineralogy of chloritoid–biotite schist (bulk compositions were determined using X-ray fluorescence (XRF) at the University of Bonn, Germany), modelling was performed on the NCMnKFMASHO system. The value of H_2O was arbitrarily fixed at 3 wt% for the construction of P–T pseudosections; an enhanced H_2O value does not change the overall topological relationships. TiO_2 was excluded from the system as it was effectively fixed in ilmenite and occurs only in very small concentrations in phyllosilicates (Tables 3, 6 & 7). It was expected that discarding TiO_2 from the system component would not have any major impact on the relative phase relations (Wei & Powell 2004; Jerabek *et al.* 2008). For the P–T pseudosections, the bulk composition of two samples of chloritoid–biotite schist, viz. #L5A/1 and #K3CG/1, were chosen (Fig. 8). In phase diagrams, both of the samples were seen to develop the critical assemblage garnet–chlorite–chloritoid–biotite at a pressure above 6 kbar and at temperatures of between 450–525 and 450–550 °C in #L5A/1 and #K3CG/1, respectively (Fig. 8). These P–T values are in good agreement with the P–T values of approximately 6.3 ± 1 kbar and 490 ± 40 °C estimated using quantitative geothermobarometry. It is intriguing to note that the assemblage in which garnet–chlorite–chloritoid–biotite are stable forms a narrow band with a conspicuous negative P–T slope. In both of the P–T pseudosections, chloritoid + biotite- and garnet + chlorite-bearing pentavariant assemblages occur on the low- and high-pressure sides of this quadrivariant band, respectively (Fig. 8a, b). The dispositions of these quadri- and pentavariant assemblages are in good agreement with the negative slope of the KFMASH univariant reaction (Als, St), with garnet + chlorite on the high-pressure side of the univariant reaction (Fig. 7).

To demonstrate the control of bulk Mn, μ_{H_2O} and μ_{O_2} in metamorphic fluid on the stability of the critical assemblage garnet–chlorite–chloritoid–biotite, the following diagrams are computed using the bulk compositions of sample #K3CG/1 as the monitor:

- isothermal–isobaric μ_{H_2O} v. μ_{O_2} diagrams at different temperatures (Fig. 9b–d);
- T (°C) v. MnO diagram, where the temperature was varied along a geothermal gradient (24 °C km^{-1}) that passes through the P–T box (*c.* 6.3 ± 1 kbar and 490 ± 40 °C) computed for the peak pressure and temperature of the area (Fig. 9a). To construct this diagram the concentration of MnO was varied from 0.00 to 1.00 wt%, keeping the concentration of other oxides in #K3CG/1 constant.

In the T (°C) v. MnO diagram, the garnet–chlorite–chloritoid–biotite-bearing assemblage has a wide stability field between 450 and 500 °C, covering the entire range of MnO (Fig. 9a). The stability field of the assemblage shrinks and is replaced with garnet–chloritoid–biotite at higher levels of MnO (>0.50 wt%) (Fig. 9a). This four-phase assemblage, therefore, stabilizes at a higher temperature range (475–500 °C) in rocks with a MnO-rich bulk composition (Fig. 9a). This feature also explains the relatively higher thermometric value yielded

Downloaded from http://sp.lyellcollection.org/ at Pennsylvania State University on September 16, 2016

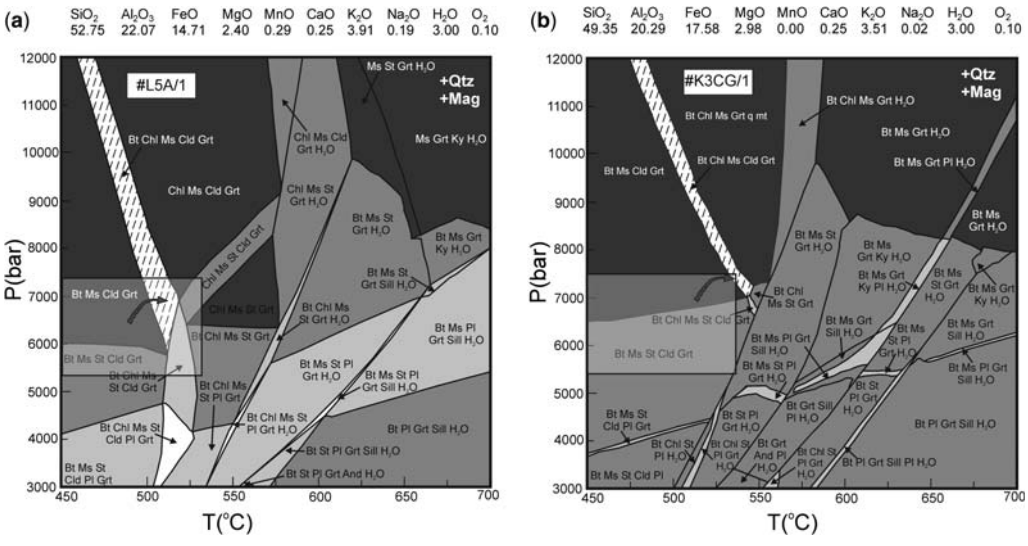

Fig. 8. *P–T* pseudosections constructed from bulk chemical compositions of two representative samples of chloritoid–biotite schists in the NCMnKFMASHO system. Bulk compositions are given above the figures. The transparent rectangle represents the *P–T* range estimated from quantitative geothermobarometry. The thick line with an arrowhead represents the likely *P–T* path that was followed by the chloritoid–biotite schists.

by the Mn-rich sample # L5A/1 than the Mn-impoverished sample # K3CG/1 (Table 8). The phase relation in the *T*–MnO diagram, therefore, explains the stabilization of the critical four-phase assemblage in #K3CG/1 within the range of estimated peak *P–T* conditions of 6.3 ± 1 kbar and 490 ± 40 °C.

In the $\mu_{H_2O}-\mu_{O_2}$ diagram, constructed at 6 kbar and 475 °C, the assemblage garnet–chlorite–chloritoid–biotite–magnetite has a very narrow wedge-shaped field (Fig. 9b). At lower and higher μ_{O_2} values, the five-phase assemblage gives way to garnet–chloritoid–biotite–magnetite and garnet–chloritoid–chlorite–magnetite, respectively (Fig. 9b). The assemblage garnet–chloritoid–biotite–chlorite ± magnetite becomes unstable at lower μ_{H_2O} irrespective of the μ_{O_2} of the metamorphic fluids (Fig. 9b). The stability field of the four- and five-phase assemblages (garnet–chloritoid–biotite–chlorite ± magnetite) shrinks at higher temperatures (Fig. 9c) and completely disappears at 550 °C (Fig. 9d).

It is evident from the above analyses that, barring pressure and temperature, several factors such as Mn in the bulk chemical composition of the rock, and the and the chemical potentials of H_2O and O_2 (μ_{H_2O} and μ_{O_2}, respectively) of the metamorphic fluid, exert a strong control on the stabilization of the critical assemblages garnet–chlorite–chloritoid–biotite in pelites. This study also demonstrates that the effects of μ_{H_2O} and μ_{O_2} can be so strong that they may obliterate the effects of other physico-chemical parameters. The net influence of these entire parameters make this assemblage a rare occurrence in medium- grade metapelites.

Discussion

Metamorphic P–T *path and their geodynamic significance*

When interpreted in the reaction topology of the KFMASH system and in the pseudosections in the system NCMnKFMASHO, textural relationships deduced for the chloritoid–biotite schist define a clockwise *P–T* path of evolution, with P_{max} preceding or reached at the same time as T_{max} (Figs 7 & 8a, b). The results of the quantitative geothermobarometry indicate that T_{max} was close to 490 ± 40 °C at a pressure of 6.3 ± 1 kbar. In view of the geometry of the *P–T* path it is, however, not possible to confirm whether the estimated pressure was equal or lower than the P_{max} of metamorphism of the studied areas. Metamorphism along a clockwise *P–T* path is generally explained in term of a subduction–obduction tectonic model commonly observed in the fold belts formed at the periphery of two or more cratonic blocks (England & Thompson 1984; Ernst 1988; Brown 1995; Goscombe *et al.* 2003).

Detailed structural analyses coupled with limited petrological studies have demonstrated that the

Downloaded from http://sp.lyellcollection.org/ at Pennsylvania State University on September 16, 2016

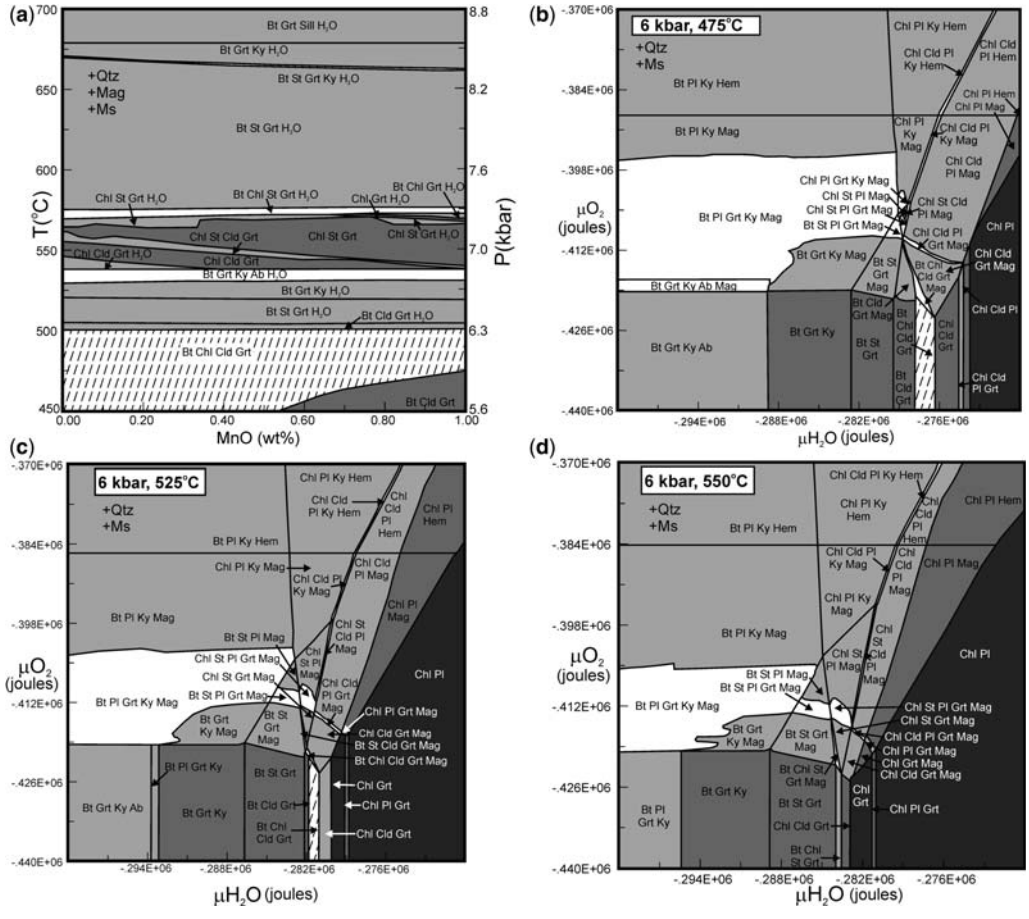

Fig. 9. (**a**) Effects of the variation of Mn and (**b**)–(**d**) μ_{H_2O} and μ_{O_2} on the stability of the chloritoid–biotite–garnet–chlorite assemblage. The bulk chemical composition of #K3CG/1 was used to construct all of the pseudosections in this figure. Note that: (a) the stability of the four–phase assemblage, which is stable between 450 and 500 °C, shrinks and is replaced by garnet–chloritoid–biotite in Mn-rich bulk conditions; and (b) the assemblages garnet–chlorite–chloritoid–biotite $\pm$ magnetite have a narrow stability field in the isothermal–isobaric $\mu_{H_2O}-\mu_{O_2}$ diagram; (c) which is further reduced at higher temperatures; and (d) eventually vanishes at a temperature close to 550 °C.

rocks in the SSZ and in the adjoining parts of the NSFB share a common structural and metamorphic history, with the localization of strain in the SSZ occurring in response to a strong compression across the interface between the NSFB and the Singhbhum Craton (Naha 1965; Sarkar 1984; Ghosh & Sengupta 1990; Mukhopadhyay & Deb 1995; Sengupta *et al.* 2005; Ghosh *et al.* 2006). Furthermore, the geometry of the kinematic markers in the SSZ confirms a thrust movement towards the south and SW as the rocks of the NSFB override the Singhbhum Craton (Fig. 1). The SSZ, which represents the lowermost part of the NSFB and is characterized by strong crystalloblastic deformation, marks the main dislocation zone between the NSFB and the Singhbhum Craton (Ghosh & Sengupta 1990). These structural attributes together with the growth of porphyroblasts during and subsequent to the development of pervasive planar fabric in the SSZ are, thus, consistent with a clockwise P–T trajectory inferred from the petrological studies.

The estimated T_{max} of 490 $\pm$ 40 °C is much higher than the temperature expected from the Precambrian geothermal gradient in the shield areas at the estimated pressure of 6.3 $\pm$ 1 kbar (Fig. 10), which, by implication, points to thermal perturbation during metamorphism (Ganguly *et al.* 1995). Studies have shown that regional metamorphism in the collisional setting is caused

Downloaded from http://sp.lyellcollection.org/ at Pennsylvania State University on September 16, 2016

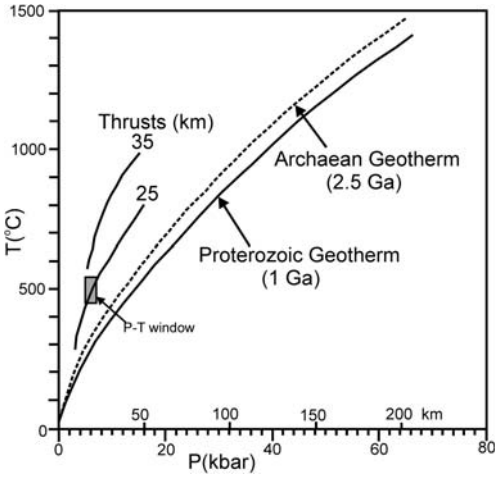

Fig. 10. Proterozoic and Archaean geotherms of the southern Indian Shield area and the perturbation of the latter due to the overthrusting of 35 and 25 km crustal blocks, as calculated by Ganguly *et al.* (1995), assuming a constant basal heat flux of 21.3 mW m^{-2} and a constant uplift rate of 0.1 mm $year^{-1}$. Note that the P–T box estimated in this study falls on the transient geothermal gradient calculated for the 25 km-thick thrust slice.

by either or both of the following heating mechanisms:

- magmatism as a consequence of the delamination of the subcrustal lithosphere (Cook *et al.* 1998);
- heat energy released by the decay of an enhanced concentration of radionuclides in the overthickened continental crust (England & Thompson 1984; Senthil Kumar *et al.* 2006).

In the absence of any synmetamorphic magmatic rocks in the studied areas, the first possibility cannot be invoked to explain the required thermal perturbation. Ganguly *et al.* (1995) computed a number of transient geothermal gradients that may develop in a collisional tectonic setting due to the decay of radionuclides for a set of thicknesses, uplift rates and internal heat generation values for the thickened crust (Fig. 10). The estimated P–T values that are constrained for the peak metamorphism of the studied area fall on the transient geothermal gradient calculated for a region that is overridden by 25 km-thick continental crust (Fig. 10). This observation, therefore, suggests that the decay of radioactive elements in 20–25 km-thick (corresponding to the pressure of 6.3 $\pm$ 1 kbar) slabs of the NSFB were sufficient to raise the temperature of metamorphism of the rocks in the SSZ to 490 $\pm$ 40 °C.

Limited geochronological data suggest that the protoliths of the metasedimentary rocks of the NSFB were deposited after 2.2 Ga, and major phases of deformation and metamorphism in the SSZ occurred in the time span of 1.5–1.8 Ga, with the main phase of shearing occurring at around 1.6 Ga (Sarkar 2000; Sengupta *et al.* 2005; Mahato *et al.* 2008). Integrating the geochronological data with the petrological information of this communication, an approximate 1.6 Ga age is tentatively assumed to be the timing of the inferred clockwise P–T path along which the Palaeoproterozoic supracrustal rocks of the NSFB and SSZ were metamorphosed. Precise geochronological work in the SSZ and in the adjoining parts of the NSFB is warranted to fix an accurate time frame of tectonothermal events in the region.

The author is indebted to Prof. D. Mukhopadhyay for his guidance in the field and during preparation of the manuscript. I thank Prof. S. C. Sarkar, Dr A. Gupta and Prof. P. Sengupta of the Department of Geological Sciences, Jadavpur University and Dr A. Matin, Department of Geology, University of Calcutta for their encouragement and many erudite discussions in the field. I am grateful to Prof. M. M. Raith and Prof. C. Ballhaus, director of the institute for allowing me to generate analytical data used for this work at the Mineralogisch Petrologisches Institut, Bonn University. Funding for fieldwork was sourced from DST Women Scientist Project 2006 awarded to the author. I convey my sincere thanks to Profs R. Mazumder and D. Saha for inviting me to write this manuscript. This work has been greatly benefited by constructive reviews from Prof. J. Ganguly and Dr I. Braun.

References

Ahn, K. S. & Nakamura, Y. 2000. The natural reaction muscovite + chlorite + chloritoid = andalusite + biotite + quartz + H_2O and a new petrogenetic grid. *Geosciences Journal*, **4**, 25–39.

Albee, A. L. 1965. A petrogenetic grid for the Fe–Mg silicates of pelitic schists. *American Journal of Sciences*, **263**, 512–536.

Albee, A. L. 1972. Metamorphism of pelitic schists: reaction relations of chloritoid and staurolite. *Geological Society of America Bulletin*, **83**, 3249–3268.

Andriessen, P. A. M., Boelrijk, N. A. I. M., Hebeda, E. H., Priem, H. N. A., Verdurmen, E. A. Th. & Verschure, R. H. 1979. Dating the events of metamorphism and granitic magmatism in the Alpine Orogen of Naxos (Cyclades, Greece). *Contributions to Mineralogy and Petrology*, **69**, 215–225.

Babůrek, J. 1998. Chloritoid Biotite Assemblage as a witness of intermediate MP/LP metamorphism in the Královský Hovzd Unit, Moldanubicum, Bohemian massif. *Geolines*, **6**, 8–9.

Baltatzis, E. & Wood, B. J. 1977. The occurrence of paragonite in chloritoid schists from Stonehaven, Scotland. *Mineralogical Magazine*, **41**, 211–216.

Bandyopadhyay, N. 2003. *Metamorphic History of the Rocks in the Southeastern Sector of the Proterozoic*

Downloaded from http://sp.lyellcollection.org/ at Pennsylvania State University on September 16, 2016

Singhbhum Shear Zone and its Environs. Unpublished PhD thesis, University of Calcutta.

Bickle, M. J. & Archibald, N. J. 1984. Chloritoid and staurolite stability: implications for metamorphism in the Archaean Yilgarn Block, western Australia. *Journal of Metamorphic Geology*, **2**, 179–203.

Brown, M. 1995. P–T–t evolution of orogenic belts and the causes of regional metamorphism. *In*: Le Bas, M. J. (ed.) *Milestones in Geology*. Geological Society of London, London, Memoirs, **16**, 67–81.

Chatterjee, N., Banerjee, M., Bhattacharya, A. & Maji, A. K. 2010. Monazite chronology, metamorphism–anatexis and tectonic relevance of the mid-Neoproterozoic Eastern Indian Tectonic Zone. *Precambrian Research*, **179**, 99–120.

Chopin, C., Seidel, E., Theye, T., Ferraris, G., Ivaldi, G. & Catti, M. 1992. Magnesiochloritoid, and the Fe–Mg series in the chloritoid group. *European Journal of Mineralogy*, **4**, 67–76.

Connolly, J. A. D. 2005. Computation of phase equilibria by linear programming: a tool for geodynamic modeling and its application to subduction zone decarbonation. *Earth and Planetary Science Letters*, **236**, 524–541.

Cook, F. A., van der Velden, A. J., Hall, K. W. & Roberts, B. J. 1998. Tectonic delamination and subcrustal imbrication of the Precambrian lithosphere in northwestern Canada mapped by LITHOPROBE. *Geology*, **26**, 839–842.

Dasgupta, S., Chakraborty, S. & Neogi, S. 2009. Petrology of an inverted Barrovian sequence of metapelites in Sikkim Himalaya, India: constraints on the tectonics of inversion. *American Journal of Science*, **309**, 43–84.

Dickenson, M. P. 1988. Local and regional differences in the chemical potential of water in amphibolite facies pelitic schists. *Journal of Metamorphic Geology*, **6**, 365–381.

Dickenson, M. P. & Hewitt, D. A. 1986. A garnet–chlorite geothermometer. *Geological Society of America, Abstracts with Programs*, **18**, 584.

Droop, G. T. R. 1987. A general equation for estimating Fe^{3+} concentrations in ferromagnesian silicates and oxides from microprobe analyses, using stoichiometric criteria. *Mineralogical Magazine*, **51**, 431–435.

Droop, G. T. R. & Harte, B. 1995. The effect of Mn on the phase relations of medium grade pelites: constraints from natural assemblages on petrogenetic grid topology. *Journal of Petrology*, **36**, 1549–1578.

England, P. C. & Thompson, A. B. 1984. Pressure–temperature–time paths of regional metamorphism: I. Heat transfer during the evolution of regions of thickened continental crust. *Journal of Petrology*, **25**, 894–928.

Ernst, W. G. 1988. Tectonic history of subduction zones inferred from retrograde blueschist P–T paths. *Geology*, **16**, 1081–1084.

Ganguly, J. 1968. Analysis of the stabilities of chloritoid and staurolite and some equilibria in the system $FeO–A1_2O_3–SiO_2–H_2O–O_2$. *American Journal of Sciences*, **266**, 277–298.

Ganguly, J. 1972. Staurolite stability and related parageneses: theory, experiments and applications. *Journal of Petrology*, **13**, 335–365.

Ganguly, J. & Saxena, S. K. 1984. Mixing properties of aluminosilicate garnets: constraints from natural and experimental data, and application to geothermobarometry. *American Mineralogist*, **69**, 88–97.

Ganguly, J., Cheng, W. & Tirone, M. 1996. Thermodynamics of aluminosilicate garnet solid solution: new experimental data, an optimized model, and thermometric applications. *Contributions to Mineralogy and Petrology*, **126**, 137–151.

Ganguly, J., Dasgupta, S., Cheng, W. & Neogi, S. 2000. Exhumation history of a section of the Sikkim Himalayas, India: records in the metamorphic mineral equilibria and compositional zoning in garnet. *Earth and Planetary Science Letters*, **183**, 471–486.

Ganguly, J., Singh, R. N. & Ramana, D. V. 1995. Thermal perturbation during charnockitization and granulite facies metamorphism in southern India. *Journal of Metamorphic Geology*, **13**, 419–430.

Ghent, E. D., Stout, M. V., Black, P. M. & Brothers, R. N. 1987. Chloritoid bearing rocks associated with blueschists and eclogites, northern New Caledonia. *Journal of Metamorphic Geology*, **5**, 239–254.

Ghosh, S. K. & Sengupta, S. 1987. Progressive development of structures in a ductile shear zone. *Journal of Structural Geology*, **9**, 277–287.

Ghosh, S. K. & Sengupta, S. 1990. Singhbhum shear zone: structural transition and kinematic model. *Proceedings of the Indian Academy of Sciences (Earth and Planetary Sciences)*, **99**, 229–247.

Ghosh, M., Mukhopadhyay, D. & Sengupta, P. 2006. Pressure–temperature–deformation history for a part of the Mesoproterozoic fold belt in North Singhbhum, Eastern India. *Journal of Asian Earth Sciences*, **26**, 555–574.

Goscombe, B., Hand, M., Gray, D. & Mawby, J. 2003. The metamorphic architecture of a transpressional Orogen: the Kaoko Belt, Namibia. *Journal of Petrology*, **44**, 679–711.

Grambling, J. A. 1983. Reversals in Fe–Mg partitioning between chloritoid and staurolite. *American Mineralogist*, **68**, 373–388.

Grambling, J. A. 1990. Internally consistent geothermometry and H_2O barometry in metamorphic rocks: the example garnet–chlorite–quartz. *Contributions to Mineralogy and Petrology*, **105**, 617–628.

Harte, B. & Hudson, N. F. C. 1979. Pelitic facies series and the temperatures and pressures of Dalradian metamorphism in eastern Scotland. *In*: Harris, A. L., Holland, C. H. & Leake, B. E. (eds) *The Celadonides of the British Isles: Reviewed*. Geological Society, London, Special Publications, **8**, 323–337.

Hiroi, Y. 1983. Progressive metamorphism of the Unazuki pelitic schists in the Hida terrane, central Japan. *Contributions to Mineralogy and Petrology*, **82**, 334–350.

Holdaway, M. J. 2000. Application of new experimental and garnet Margules data to the garnet–biotite geothermometer. *American Mineralogist*, **85**, 881–892.

Holdaway, M. J., Dutrow, B. L. & Hinton, R. W. 1988. Devonian and Carboniferous metamorphism in west-central Maine: the muscovite–almandine geobarometer and the staurolite problem revisited. *American Mineralogist*, **73**, 20–47.

Holland, T. J. B. & Powell, R. 1998. An internally consistent thermodynamic data set for phases of

Downloaded from http://sp.lyellcollection.org/ at Pennsylvania State University on September 16, 2016

petrological interest. *Journal of Metamorphic Geology*, **16**, 309–343.

HOLLAND, T., BAKER, J. & POWELL, R. 1998. Mixing properties and activity–composition relationships of chlorites in the system $MgO–FeO–Al_2O_3–SiO_2–H_2O$. *European Journal of Mineralogy*, **10**, 395–406.

HYNES, A. & FOREST, R. C. 1988. Empirical garnet–muscovite geothermometry in low-grade metapelites, Selwyn Range (Canadian Rockies). *Journal of Metamorphic Geology*, **6**, 297–309.

JERABEK, P., JANAK, M. K., FARYAD, S. W., FINGER, F. & KONECNY, P. 2008. Polymetamorphic evolution of pelitic schists and evidence for Permian low-pressure metamorphism in the Vepor Unit, West Carpathians. *Journal of Metamorphic Geology*, **26**, 465–485.

KALT, A., ALTHERR, R. & LUDWIG, T. 1998. Contact metamorphism in pelitic rocks on the island of Kos (Greece, Eastern Aegean Sea): a test for the Na-in cordierite thermometer. *Journal of Petrology*, **39**, 663–668.

KRETZ, R. 1983. Symbols for rock forming minerals. *American Mineralogist*, **68**, 277–279.

LABOTKA, T. C. 1980. Petrology of a medium pressure regional metamorphic terrain, Funeral Mountains, California. *American Mineralogist*, **65**, 670–689.

LABOTKA, T. C. 1981. Petrology of an andalusite type regional metamorphic terrain, Paramint Mountains, California. *Journal of Petrology*, **22**, 261–296.

LIKHANOV, I. I., REVERDATTO, V. V., SHEPLEV, V. S., VERSCHININ, A. E. & KOZLOV, P. S. 2001. Contact metamorphism of the Fe and Al-rich metapelites in the Transangarian region of the Yenisei Ridge, eastern Siberia, Russia. *Lithos*, **58**, 55–80.

LOOMIS, T. P. 1986. Metamorphism of metapelites: calculations of equilibrium assemblages and numerical simulations of the crystallization of garnet. *Journal of Metamorphic Geology*, **4**, 201–229.

MAHATO, S., GOON, S., BHATTACHARYA, A., MISHRA, B. & BERNHARDT, H. J. 2008. Thermo-tectonic evolution of the North Singhbhum Mobile Belt (eastern India): a view from the western part of the belt. *Precambrian Research*, **162**, 102–127.

MPOSKOS, E. 1989. High-Pressure metamorphism in gneisses and pelitic schists in the East Rhodope Zone (N. Greece). *Mineralogy and Petrology*, **41**, 25–39.

MUKHOPADHYAY, D. & DEB, G. 1995. Structural and textural development in Singhbhum shear zone, eastern India. *Proceedings of the Indian Academy of Sciences (Earth and Planetary Sciences)*, **104**, 385–405.

NAHA, K. 1965. Metamorphism in relation to stratigraphy, structure and movements in part of East Singhbhum, Eastern India. *Quarterly Journal of the Geological, Mineralogical and Metallurgical Society of India*, **37**, 41–88.

NEWTON, R. C., CHARLU, T. V. & KLEPPA, O. J. 1980. Thermochemistry of the high structural state plagioclases. *Geochimica et Cosmochimica Acta*, **44**, 933–941.

PERCHUK, L. L. & LAVRENTIEVA, I. V. 1983. Experimental investigation of exchange equilibria in the system cordierite–garnet–biotite. *In*: SAXENA, S. K. (ed.) *Kinetics and Equilibrium in Mineral Reactions*. Advances in Physical Geochemistry, **3**, 199–239.

PITRA, P. & GUIRAUD, M. 1996. Probable anticlockwise P–T evolution in extending crust: Hlinsko region, Bohemian Massif. *Journal of Metamorphic Geology*, **14**, 49–60.

POUCHOU, L. & PICHOIR, F. 1984. A new model for quantitative X-ray microanalysis, Part-I: Application to the analysis of homogeneous samples. *La Recherche Aérospatiale*, **3**, 167–192.

POWELL, R. & HOLLAND, T. 1990. Calculated mineral equilibria in the pelite system, KFMASH ($K_2O–FeO–MgO–Al_2O_3–SiO_2–H_2O$). *American Mineralogist*, **75**, 367–380.

POWELL, R. & HOLLAND, T. 1999. Relating formulations of the thermodynamics of mineral solid solutions: activity modeling of pyroxenes, amphiboles, and micas. *American Mineralogist*, **84**, 1–14.

RAO, N. K. & RAO, G. V. U. 1983. Uranium mineralization in Singhbhum shear zone, Bihar: IV. Origin and geological time frame. *Journal of the Geological Society of India*, **24**, 615–627.

ROY, A., SARKAR, A., JEYAKUMAR, S., AGGRAWAL, S. K. & EBIHARA, M. 2002. Sm–Nd age and mantle source characteristics of the Dhanjori volcanicrocks, Eastern India. *Geochemical Journal*, **36**, 503–518.

SAHA, A. K. 1994. *Crustal Evolution of Singhbhum–North, Orissa, Eastern India*. Geological Society of India, Memoirs, **27**.

SARKAR, S. C. 1984. *Geology and Ore Mineralisation Along the Singhbhum Copper–Uranium Belt, Eastern India*. Jadavpur University, Calcutta.

SARKAR, S. C. 2000. Crustal evolution and metallogeny in the eastern Indian craton. *In*: *National Seminar Commemorating Dr M. S. Krishnan's Birth centenary (Proceedings Volume)*. Geological Survey of India, Special Publications, **55**, 169–194.

SENGUPTA, N., MUKHOPADHYAY, D., SENGUPTA, P. & HOFFBAUER, R. 2005. Tourmaline-bearing rocks in the Singhbhum shear zone, eastern India: evidence of boron infiltration during regional metamorphism. *American Mineralogist*, **90**, 1241–1255.

SENTHIL KUMAR, P., MENON, R. & REDDY, G. K. 2006. The role of radiogenic heat production in the thermal evolution of a Proterozoic granulite–facies orogenic belt: Eastern Ghats, Indian Shield. *Earth and Planetary Science Letters*, **254**, 39–54.

SHARMA, M., BASU, A. R. & RAY, S. L. 1994. Sm–Nd isotopic and geochemical study of the Archaean tonalite–amphibolite association from the eastern India craton. *Contributions to Mineralogy and Petrology*, **117**, 45–55.

SHARMA, R. S. 2010. *Cratons and Fold Belts of India*. Lecture Notes in Earth Sciences, **127**, doi: 10.1007/978-3-642-01459-8_2.

SPEAR, F. S. 1993. *Metamorphic Phase Equilibria and Pressure–Temperature–Time Paths*. Mineralogical Society of America, Washington, DC.

SPEAR, F. S. & CHENEY, J. T. 1989. A petrogenetic grid for pelitic schists in the system $SiO_2–Al_2O_3–FeO–MgO–K_2O–H_2O$. *Contributions to Mineralogy and Petrology*, **101**, 149–164.

TRIBOULET, C. 1983. Uni- and divariant equilibria between staurolite, chloritoid, garnet, chlorite, biotite in medium pressure meta-acidites from Lorient-Concarneau area (South Brittany, France). *Contributions to Mineralogy and Petrology*, **82**, 195–204.

Downloaded from http://sp.lyellcollection.org/ at Pennsylvania State University on September 16, 2016

WANG, P. & SPEAR, F. S. 1991. A field and theoretical analysis of garnet + chlorite + chloritoid + biotite assemblages from the tri-state (MA, CT, NY) area, USA. *Contributions to Mineralogy and Petrology*, **106**, 217–235.

WATERS, D. J. & LOVEGROVE, D. P. 2002. Assessing the extent of disequilibrium and overstepping of prograde metamorphic reactions in metapelites from the Bushveld Complex aureole, South Africa. *Journal of Metamorphic Geology*, **20**, 135–149.

WEI, C. J. & POWELL, R. 2004. Calculated phase relations in high-pressure metapelites in the system NKFMASH (Na_2O–K_2O–FeO–MgO–Al_2O_3–SiO_2–H_2O) with application to natural rocks. *Journal of Petrology*, **44**, 183–202.

WHITNEY, D. L., MECHUM, T. A., KUEHNER, S. M. & DILEK, Y. R. 1996. Progressive metamorphism of pelitic rocks from protolith to granulite facies, Dutchess County, New York, USA: constraints on the timing of fluid infiltration during regional metamorphism. *Journal of Metamorphic Geology*, **14**, 163–181.

WU, C. M. & ZHAO, G. 2006. Recalibration of the Garnet–Muscovite (GM) geothermometer and the Garnet–Muscovite–Plagioclase–Quartz (GMPQ) geobarometer for metapelitic assemblages. *Journal of Petrology*, **47**, 2357–2368.

WU, C. M., ZHANG, J. & REN, L. D. 2004. Empirical Garnet–Biotite–Plagioclase–Quartz (GBPQ) geobarometry in medium- to high-grade metapelites. *Journal of Petrology*, **45**, 1907–1921.

ZANE, A., SASSI, R. & GUIDOTTI, C. V. 1998. New data on metamorphic chlorite as a petrogenetic indicator mineral, with special regard to greenschist-facies rocks. *The Canadian Mineralogist*, **36**, 713–726.